Atmos. Meas. Tech., 19, 3961–3982, 2026
https://doi.org/10.5194/amt-19-3961-2026

Atmospheric Measurement Techniques
Open Access

Measuring molecular singlet oxygen ($^1O_2^*$) from atmospheric photosensitizers: Intercomparison of techniques, irradiation setups, data analysis and protocol recommendations

Keighan J. Gemmell[1], Laura Marie Dahler Heinlein[2], Emma A. Petersen-Sonn[3], Claudia Sardena[1], Zhongyu Guo[3], Nory Mariño-Ocampo[4], Belinda Heyne[4], Christian George[3], Cort Anastasio[2], and Nadine Borduas-Dedekind[1]

[1]Department of Chemistry, University of British Columbia, Vancouver, V6T 1Z1, Canada
[2]Department of Land, Air and Water Resources, University of California, Davis, CA 95616, USA
[3]Universite Claude Bernard Lyon 1, CNRS, IRCELYON, UMR 5256, Villeurbanne, 69100, France
[4]Department of Chemistry, University of Calgary, 2500 University Drive NW, Calgary, AB T2N 1N4, Canada

Correspondence: Nadine Borduas-Dedekind (borduas@chem.ubc.ca)

Received: 19 December 2025 – Discussion started: 28 January 2026
Revised: 20 April 2026 – Accepted: 11 May 2026 – Published: 17 June 2026

Abstract. Molecular singlet oxygen ($^1O_2^*$) is the first excited state of molecular oxygen (O_2) and can be formed through indirect photochemistry during irradiation of chromophoric organic matter. Once formed in the particle and droplet phases in the atmosphere, $^1O_2^*$ can be a competitive oxidant in the photochemical processing of organic matter. Now, as more researchers study the atmospheric photochemistry of $^1O_2^*$, establishing protocols by evaluating and comparing experimental setups across laboratories is becoming necessary. Here, we present $^1O_2^*$ measurements from four photosensitizing molecules in four photoreactor setups at three research institutions, including two xenon lamps of different strengths and two multi-bulb UVA + UVB broadband systems. The production of $^1O_2^*$ was investigated from perinaphthenone, lignin, and juglone, which are photosensitizers with atmospherically relevant light absorbing moieties, as well as from Rose Bengal, a standard photosensitizer. Two chemical actinometers, 2-nitrobenzaldehyde and p-nitroanisole/pyridine, were used to quantify photon fluxes and calculate rates of light absorbance for photosensitizers for each photoreactor. We compared two commonly used $^1O_2^*$ quantification methods, chemical probe method using furfuryl alcohol, as well as direct $^1O_2^*$ phosphorescence detection at 1270 nm. Rates of light absorbance across experimental setups for each photosensitizer ranged between 0.2 and 62×10^{-5} $\mathrm{mol_{photons}\,L^{-1}\,s^{-1}}$, while $^1O_2^*$ steady-state concentrations ranged between 0.01 and 129×10^{-11} M. Despite order of magnitude differences in rate of light absorbance and $^1O_2^*$ steady state concentrations, normalizing to $^1O_2^*$ quantum yields showed good inter-laboratory agreement but only for the sensitizers with high quantum yields: perinaphthenone (94 % ± 9 %–112 % ± 17 %) and for Rose Bengal (67 % ± 15 %–87 % ± 5 %). $^1O_2^*$ quantum yields for lignin and juglone increased with decreasing irradiation wavelength, highlighting a wavelength-dependence. Finally, we make five recommendations to improve the accuracy and reproducibility of $^1O_2^*$ measurements for the atmospheric chemistry community. These recommendations include considering wavelength-dependent quantum yields, avoiding suppression of $^1O_2^*$, controlling and reporting photoreactor temperature, considering light scattering from nanoparticles, and conducting control experiments. These recommendations can serve as guidelines to build future photoreactors as well as help standardize $^1O_2^*$ measurements in studying photochemical processing of atmospheric aerosols and droplets.

1 Introduction

Wildfires are becoming more frequent and severe with rising global temperatures, affecting air quality, climate, and human health (Tymstra et al., 2020). These events are major sources of brown carbon (BrC) aerosols, which contain light-absorbing organic chromophores capable of driving complex photochemistry in the atmosphere (Laskin et al., 2015). Upon absorbing sunlight, these chromophores reach electronically excited states that can transfer energy to other atmospheric species, initiating indirect oxidation pathways (George et al., 2015; Li et al., 2022; Hems et al., 2021). One particularly important pathway is the formation of triplet excited state organic carbon ($^3C^*$) and its subsequent energy transfer to molecular oxygen, generating singlet oxygen ($^1O_2^*$), a potent oxidant (Kaur and Anastasio, 2018; McNeill and Canonica, 2016). Excited-state oxidants have been hypothesized to contribute to the elevated oxidation state of carbon observed in wildfire plumes, beyond what can be explained by classical radical chemistry (Akherati et al., 2022).

$^1O_2^*$ is efficiently generated by well-characterized synthetic photosensitizers such as Rose Bengal and Methylene Blue (Wilkinson et al., 1993), including within the context of photo-dynamic therapy (Gianotti et al., 2014; Dhaini et al., 2022). In natural waters, dissolved organic matter is a strong photosensitizer, with quinones, aldehydes, ketones, coumarins, and polycyclic aromatic hydrocarbons among the compound classes responsible for $^1O_2^*$ production (McNeill and Canonica, 2016). Atmospheric BrC contains chemical analogues of these same chromophores, including nitrophenols (Xu et al., 2022), nitroanisoles (Zheng et al., 2023; Li et al., 2025b), quinones (Lee et al., 2014), and aromatic carbonyls (Smith et al., 2014, 2016), though their photosensitizing activity remains incompletely characterized. Measurements of $^1O_2^*$ across atmospheric samples such as fog water (Anastasio and McGregor, 2001; Kaur and Anastasio, 2017), cloud and rainwater (Faust and Allen, 1992; Albinet et al., 2010), indoor cooking aerosols (Borduas-Dedekind et al., 2024), road dust (Cote et al., 2018; Burnett et al., 2025), and particulate matter extracts (Manfrin et al., 2019; Ma et al., 2023b; Lyu et al., 2023; Bogler et al., 2022; Cote et al., 2018; Kaur et al., 2019a; Leresche et al., 2021) confirm that $^1O_2^*$ is ubiquitous in multiphase atmospheric environments . Recent studies also demonstrate $^1O_2^*$ reactivity at air–solid and air–water interfaces (Durantini et al., 2023; Durantini and Greer, 2021; Li et al., 2025a).

Concentrations of $^1O_2^*$ are typically on the order of 10^{-13} M (Bogler et al., 2022; Cole et al., 2018; Kaur et al., 2019b; Leresche et al., 2021; Lyu et al., 2023; Ma et al., 2023b, a; Manfrin et al., 2019; Heinlein et al., 2025), an order of magnitude larger that its triplet excited state precursor (10^{-14} M) (Kaur et al., 2019b; Lyu et al., 2023; Ma et al., 2023b, a) and two orders of magnitude larger than •OH (10^{-15} M) (Arakaki et al., 2013; Kaur et al., 2019b; Leresche et al., 2021; Ma et al., 2023b, a; Zhou et al., 2008) in atmospheric extracts. Yet, reported $^1O_2^*$ quantum yields vary widely, even for the same material. For example, Suwannee River fulvic acid shows quantum yields ranging from 0.47 % to 5.4 %, with strong wavelength dependence (Partanen et al., 2020). Atmospheric samples likewise span 0.2 %–19 % (Ma et al., 2023a; Petersen-Sonn et al., 2025; Kaur et al., 2019b; Bogler et al., 2022; Manfrin et al., 2019; Ma et al., 2024; Lyu et al., 2023). Some of these discrepancies arise from using different rate constants, different parameters for light absorbance, dismissing the presence of competing oxidants, or measurement errors (Ossola et al., 2021).

The challenge of extrapolating laboratory measurements of $^1O_2^*$ to the atmospheric context is exacerbated by the current lack of reproducibility in environmental samples such as the Suwannee River fulvic acid samples (Partanen et al., 2020), making it difficult to distinguish between variability in $^1O_2^*$ measurements and true inconsistencies in reproducibility. Anton et al. (2024) recently reported an intercomparison study in surface water context related to photochemical processes and made suggestions on how to limit the uncertainty related to the wavelength-dependence of quantum yields. Indeed, two extensive reviews have been written in the aquatic context to help reduce measurement reporting discrepancies by Ossola et al. (2021) and Anton et al. (2024). Our study builds on their work as we consider the atmospheric context of measuring excited state oxidants.

To evaluate atmospheric measurement consistency, we selected a diverse set of BrC-relevant photosensitizers: perinaphthenone, juglone, and lignin (Fig. 1). Perinaphthenone is a benchmark $^1O_2^*$ sensitizer with well defined photophysics (Schmidt et al., 1994; Schweitzer and Schmidt, 2003) and structurally similar to BrC moieties (Samburova et al., 2016). Juglone represents hydroxyquinones which have been proposed to be atmospheric photosensitizers linked to BrC formation (Lee et al., 2014; Manfrin et al., 2019). Lignin and its derived products are present in biomass burning organic aerosols,(Myers-Pigg et al., 2016; Shakya et al., 2011) and can generate $^1O_2^*$ upon irradiation (Du et al., 2018; Fleming et al., 2020). For a standard comparison, we also included Rose Bengal as a well studied reference sensitizer commonly used to benchmark $^1O_2^*$ quantum yields, albeit an atmospherically irrelevant molecule (Redmond and Gamlin, 1999; Gottschalk et al., 1986).

Here, we quantified $^1O_2^*$ production from four photosensitizers in four photoreactor setups across three institutions to establish a standard operating procedure for atmospheric chemistry experiments. To compliment our inter-laboratory photoreactor intercomparison, we also measured $^1O_2^*$ quantum yields using phosphorescence spectroscopy to act as a method comparison to chemical probe quantification. Standardizing a method of $^1O_2^*$ measurement is timely, as the there are increasing numbers of studies of photooxidants in irradiated particulate matter (Heinlein et al., 2025; Chang et al., 2025). This study is unique in its direct intercomparison of $^1O_2^*$ quantification using the identical photosensitizing molecules and procedures across different photoreactor setups. Following this intercomparison, we provide recommendations to standardize $^1O_2^*$ measurements to minimize errors and enhance interpretation of results specifically across different light sources. Our goal is to provide a methodological road map for future studies to consider and adopt in the

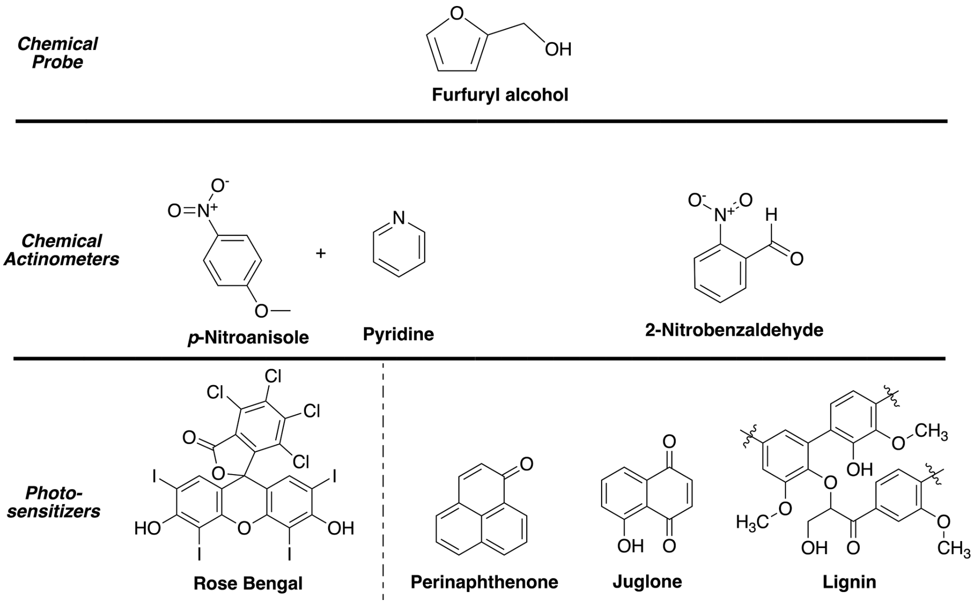

Figure 1. Structures of chemicals used in this study. Top row: chemical probe, furfuryl alcohol (FFA). Middle row: chemical actinometers, p-nitroanisole (PNA)/pyridine (Pyr), and 2-nitrobenzaldehyde (2NB). Bottom row: photosensitizers. Rose Bengal is a synthetic dye standard and perinaphthenone, juglone, and lignin are atmospherically relevant moieties.

measurements of photooxidants with a focus on $^1O_2^*$ in atmospherically relevant samples.

2 Methods

2.1 Chemicals

Isopropanol (HPLC grade, $\geq 99.9\,\%$), perinaphthenone (97 %), juglone (5-hydroxy-1,4-naphthoquinone, 97 %), lignin (low sulphonate alkali lignin), 4-nitrophenol (98 %), 2-nitroanisole (98 %), 3-nitroanisole (98 %), 4-nitroanisole (98 %), Rose Bengal (95 %), 2-nitrobenzaldehyde (2NB, 98 %), and pyridine (Pyr, $> 99.9\,\%$) were all purchased from Sigma-Aldrich and used without further purification. All solutions were prepared using 18.2 MΩ cm Milli-Q water.

Furfuryl alcohol (FFA, 97 %) and p-nitroanisole (PNA, 97 %) were checked for purity using UV-Vis, and purified if coloured impurities were present. Specifically, FFA was purified using a liquid-liquid extraction with $NaHCO_3$, followed by fractional distillation under reduced pressure (see Fig. S20 for the impact of FFA impurities on control experiments) (Armarego and Chai, 2013). FFA was then stored in the fridge and covered in foil to avoid any photochemical processes. PNA was recrystallized from petroleum ether at 60 °C (Armarego and Chai, 2013).

2.2 Instruments

In this section, we describe the details of each photoreactor at the University of British Columbia (UBC), University of California Davis (UCD), and Universite Claude Bernard Lyon 1 (Ircelyon), as well as high performance liquid chromatograph (HPLC), UV/Vis spectrometer and spectrophotometer at each institution.

2.2.1 Photoreactor experimental setups

UBC. The photoreactor used at UBC was a Rayonet RPR-200 (The Southern NE Ultraviolet Co.) equipped with 16 removable bulbs and a rotating sample carousel (Fig. 2a). The photoreactor was temperature controlled using the vented gas from a 15 L liquid nitrogen dewar (Cryofab, Inc. CLPB-15-GF). Temperature was monitored using a thermocouple probe (Thermosense BTM-4208SD 12 Channels Temperature Recorder) at each time-point. Experimental solutions (5 mL) were transferred into borosilicate glass test tubes and set into a rotating carousel. Empty slots on the carousel were filled with borosilicate glass vials containing 5 mL of MilliQ water in order to ensure homogeneous light distribution. Experimental solutions contained 20 µM furfuryl alcohol, 1 mM of isopropanol and 10 µM of either perinaphthenone, Rose Bengal, juglone, or 20 mg L^{-1} of lignin. At 6–10 designated time points during illumination, 100 µL aliquots were removed for furfuryl alcohol quantification. Two UBC photoreactor setups were used for the present study. One setup used 12 UVA centred bulbs (Southern NE Ultraviolet Co., RPR-3500A), herein referred to as UBC UVA. The other setup used 8 UVA centred bulbs and 8 UVB centred bulbs (Zoo Med 26396 Reptisun 15 W 10.0 T5-Ho UVB Fluorescent Lamp, 12 in.), herein referred to as UBC UVA+UVB broadband.

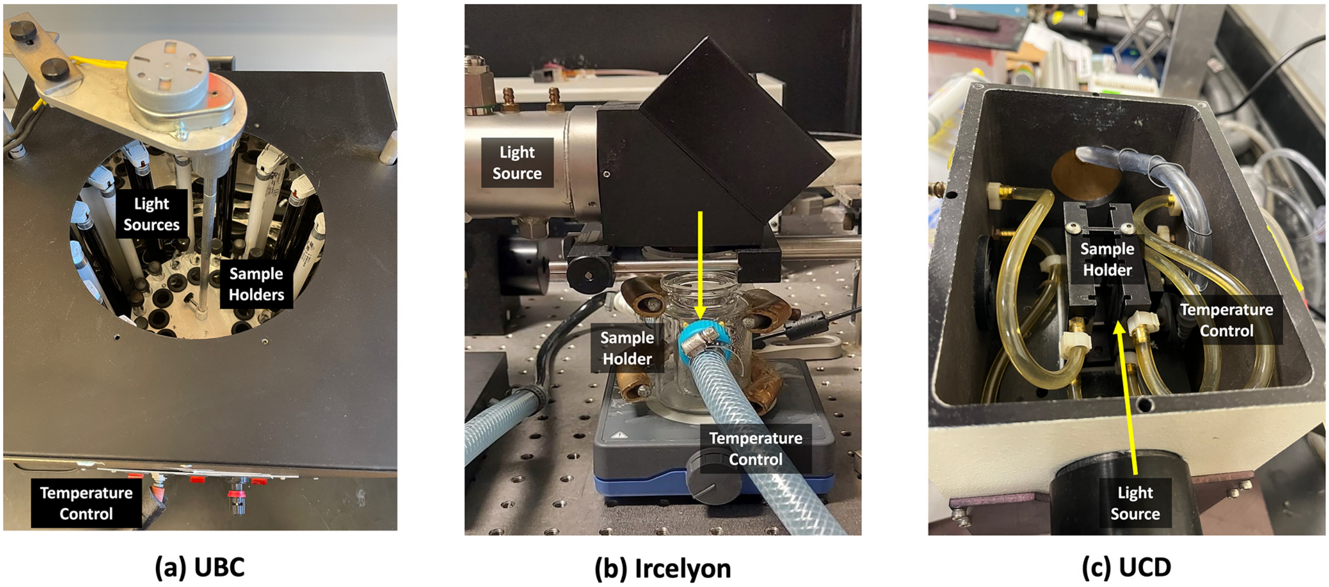

(a) UBC (b) Ircelyon (c) UCD

Figure 2. Experimental setup of 3 different laboratory photoreactors. **(a)** UBC, **(b)** Ircelyon, and **(c)** UCD. Details of each photoreactor setup are shown in Table 1. Main components of each set up, light source, sample holders, and temperature control, are labelled. Direction of light beam travel is indicated with a yellow arrow in panels **(b)** and **(c)**, and is in all directions in panel **(a)**.

UCD. At UCD, tropospheric sunlight was simulated with a 1000 W xenon arc lamp with three downstream optical filters: a water filter, an AM1.0 air mass filter (AM1D-3L, Sciencetech), and a 295 nm long-pass filter (20CGA-295, Thorlabs) (Fig. 2b). The temperature of the illumination chamber was controlled with a water bath set to 20 °C. Illuminations were either performed in 1 mL GE 021 quartz tubes (5 mm inner diameter) or in 5 mL rectangular quartz cuvettes (1 cm pathlength; Starna Cells). Experimental solutions contained 20 µM furfuryl alcohol, 1 mM of isopropanol and 10 µM of either perinaphthenone, Rose Bengal, juglone, or 20 mg L^{-1} of lignin. At five designated time points during each illumination experiment, 130 µL aliquots were removed for furfuryl alcohol quantification. For the experiments performed in 1 mL tubes, the entire solution was illuminated. The solutions did not need to be stirred during illumination but the solutions were shaken vigorously prior to aliquot removal. For the experiments performed in cuvettes, the light beam only illuminated a subset of the solution and therefore the solutions were stirred during illumination. The volume removed during the cuvette experiments did not exceed 15 % of the initial illuminated volume.

Ircelyon. The set-up applied in Ircelyon consisted of a glass photoreactor equipped with a water jacket to allow for temperature control (Fig. 2c). Experimental solutions contained 20 µM furfuryl alcohol, 1 mM of isopropanol and 10 µM of either perinaphthenone, Rose Bengal, or 30 µM juglone, or 40 mg L^{-1} of lignin. 20 mL of experimental solution were transferred to the photoreactor for irradiation. All experiments were performed at 293 K (20 °C). The solution was stirred by a magnetic stirrer. A quartz lid was placed on top of the reactor to avoid exchange with the air surrounding the set-up. The light source applied was a xenon lamp (LOT LSE140/160.25C, 150 W), which had an infrared (IR) filter, a mirror bending the light 90°, followed by a Pyrex filter to avoid light with wavelengths below 280 nm.

2.2.2 HPLC

UBC. High performance liquid chromatography (HPLC, Agilent 1260, Agilent Technologies) equipped with a photodiode array detector was used to quantify the decay of the photooxidant probes. The analytical method was conducted with a reverse phase C18 column (Agilent, 5 µm, 4.6 × 150 mm) and an eluent gradient of acetonitrile (ACN) and MilliQ water for furfuryl alcohol. For the furfuryl alcohol quantification, a flow rate of 1 mL min^{-1} was used. The gradient was 6 min at 20 / 80 (water / ACN), and 2 min at 90 / 10 (water / ACN) for a total run duration of 8 min. Furfuryl alcohol was monitored at 219 nm and typically observed at 3.32 min (Bogler et al., 2022). For the monitoring of 2-nitrobenzaldehyde, a flow rate of 0.5 mL min^{-1} was applied to an isocratic gradient of 60 / 40 (water / ACN), and maintained for 20 min. 2-nitrobenzaldehyde was monitored at 254 nm and was typically observed at 9.6 min. For p-nitroanisole, the gradient was 6 min at 50 / 50 acetonitrile/acetate buffer (pH = 6). The p-nitroanisole peak was typically quantified at 316 nm.

UCD. Furfuryl alcohol was monitored using high performance liquid chromatography (HPLC: Shimadzu LC-20AB pump, Thermo Scientific Accucore XL C18 column (50 × 3 mm, 4 µm bead), and Shimadzu-M20A Photodiode

Array detector. A flow rate of 0.45 mL min^{-1} and an eluent gradient with 2 min of 10 / 90 (acetonitrile / water), 3.5 min of 40 / 60 (acetonitrile / water), and the remaining 12.5 min with 10 / 90 (acetonitrile / water) for a total run time of 18 min was used. Furfuryl alcohol was quantified at 210 nm and eluted at 3.0 min, and the remainder of the run was to ensure all photosensitizers were flushed from the column.

Ircelyon. Samples were extracted at varying time intervals, depending on the experiment, and set aside for UHPLC/UV analysis. The method applied for UHPLC/UV analysis had an ACQUITY UPLC HSS T3 by WATERS column (100 mm × 2.1 mm, 1.8 µm) and is also described in Petersen-Sonn et al. (2024). With a flow of 0.3 mL min^{-1} the method started using two solvents: H_2O with 0.1 % formic acid (solvent A), and acetonitrile (ACN) with 0.1 % formic acid (solvent B). Initially, 1 % solvent B (and 99 % solvent A) was applied for 2 min. In the next 11 min, the gradient gradually shifted from 1 % to 100 % solvent B. After this, solvent B was kept at 100 % for the following 2 min, which was followed by a change to 1 % solvent B (over 0.1 min), which was kept until the end of the sequence (total runtime of 22 min). This allowed for an equilibrium of the column before the next sample was injected. Furfuryl alcohol, 2-nitrobenzaldehyde and p-nitroanisole were analyzed at 218, 254, and 320 nm, respectively.

2.2.3 UV/Vis spectroscopy

All absorbance spectra of experimental solutions was measured from 200–800 nm and contained furfuryl alcohol, isopropanol, the photosensitizer. Samples were measured in 1 cm pathlength quartz cuvettes, and were corrected for baseline and for the absorbance of a blank furfuryl alcohol + isopropanol solution to isolate the absorbance of the photosensitizer. At UBC, absorbance spectra were recorded using a double beam UV/Visible spectrometer (Carry 5000, Varian). At UCD, absorbance spectrum of each sample solution were measured with a Shimadzu UV-2501PC spectrophotometer. At Ircelyon, solutions were measured using an Agilent Cary 60 spectrophotometer.

2.2.4 Photospectrometers

An Ocean Optics FLAME-T-UV-VIS spectrophotometer equipped with a QP600-1-XSR fiber optic cable and a CC-3-UV-S cosine receptor was used to measure the irradiance spectrum of the photoreactor setups at UBC. Due to the rotation of the carousel sample holder, the spectrophotometer probe was positioned in one of the sample slots and rotated for measurement. One rotation of the sample carousel took 10 s. To not oversaturate the spectrophotometer detector and to obtain the entire photoreactor light output the spectrophotometer integration time was set to 0.25 s and averaged over 40 scans. At UCD, a TIDAS S 300 VIS/NIR 3011 (MMS 300–1100 nm) spectrophotometer was used to measure the irradiance spectrum of the solar simulator. The Ircelyon laboratory used an Avantes AVASPEC-HSC1024 x 58TEC-EVO spectrophotometer, equipped with an optical fiber (FC-UV/IR-400-1-PR, Avantes) that has a cosine corrector, was employed to measure the irradiance spectrum of the lamp.

2.3 Quantifying $^1O_2^*$ formation parameters

2.3.1 Rate of light absorbance

The rate of light absorbance (R_{abs}, mol$_{\text{photons}}$ L^{-1} s^{-1}) of the photosensitizer was calculated by:

$$R_{\text{abs}} = \sum_{\lambda} \left(I_{\lambda,0} \cdot \alpha_{\lambda} \cdot \Delta\lambda \cdot 2.303 \cdot 10^3 \right) \qquad (1)$$

where α_λ is light absorption coefficient of the sample (cm^{-1}, baseline corrected), $I_{\lambda,0}$ is the spectral irradiance of the light source (mol$_{\text{photons}}$ cm^{-2} s^{-1} nm^{-1}), $\Delta\lambda$ is the interval between adjacent wavelengths, and the values 2.303 and 10^3 are conversions for base and units, respectively (Kaur et al., 2019b). Following the recommendations of Ossola et al. (2021), UV-vis spectra were corrected by averaging and subtracting the absorbance of a sample from 700–800 nm (or the region of noise determined in logarithmic absorbance space of the UV-Vis spectrum) from the entire absorbance spectra. Additionally, negative absorbance values were screened and set to be 0 to avoid an artificial decrease in the rate of light absorbance. A baseline spectrum was also taken with the solvent (water) as well as isopropanol and furfuryl alcohol.

2.3.2 $^1O_2^*$ production under pseudo-first-order conditions

$^1O_2^*$ was detected using furfuryl alcohol as a chemical probe, which has a well constrained rate constant with $^1O_2^*$ of $1 \times 10^8 + 2.1 \times 10^6\ (T\,[°\mathrm{C}] - 22)\ \mathrm{M^{-1}\,s^{-1}}$ (Appiani et al., 2017) and has been used for several decades for $^1O_2^*$ quantification (Haag et al., 1984). The decay of the furfuryl alcohol probe was followed with (U)HPLC/UV. The loss of the $^1O_2^*$ probe, furfuryl alcohol, can be expressed as:

$$\begin{aligned} -\frac{\mathrm{d[FFA]}}{\mathrm{d}t} &= k_{\mathrm{FFA}+{}^1O_2^*} \times [\mathrm{FFA}] \times [{}^1O_2^*]_{\mathrm{ss}} \\ &\quad + k_{\mathrm{FFA}+{}^3C^*} \times [\mathrm{FFA}] \times [{}^3C^*]_{\mathrm{ss}} \\ &\quad + k_{\mathrm{FFA}+\bullet\mathrm{OH}} \times [\mathrm{FFA}] \times [\bullet\mathrm{OH}]_{\mathrm{ss}} + j_{\mathrm{FFA}} \end{aligned} \qquad (2)$$

The reaction of furfuryl alcohol with hydroxyl radicals (•OH) was set to be 0 due to the use of isopropanol as a quencher (Bogler et al., 2022), and the direct photodegradation (j_{FFA}) was also negligible for the irradiance times used in this study, evidenced by the direct photodegradation control experiments (Fig. S1 in the Supplement). The reaction of furfuryl alcohol with $^3C^*$ is also negligible, evidenced by deoxygenation control experiments (Fig. S2). Therefore, the loss of furfuryl alcohol can then be expressed only as a function of its reaction with $^1O_2^*$.

$$\ln\left(\frac{[\mathrm{FFA}]_t}{[\mathrm{FFA}]_0}\right) = k_{\mathrm{FFA}+^1O_2^*} \times [^1O_2^*]_{\mathrm{ss}} \times \mathrm{t} = k_{\mathrm{obs,FFA}} \times t \quad (3)$$

Through this decay, the pseudo-first-order rate constant, $k_{\mathrm{obs,FFA}}$, was obtained (Figs. S2–S7). $k_{\mathrm{obs,FFA}}$ was then corrected for light screening of the sample:

$$k_{\mathrm{obs,corr}} = \frac{k_{\mathrm{obs,FFA}}}{\mathrm{sf}} \quad (4)$$

2.3.3 Light screening factor

Internal light screening due to light absorption is the reduction of light intensity within a sample as photons are absorbed before they can reach the entire irradiated volume. The light screening of the sample depends on the light absorbance of the sample, the path length of the light through the sample, and the irradiance from the light source. The light screening factor (sf) is described by Eq. (5).

$$\mathrm{sf} = \frac{\sum\left((1-10^{-\alpha_\lambda \cdot l})I_{\lambda,0}\right)}{\sum(2.3 \cdot \alpha_\lambda \cdot l \cdot I_{\lambda,0})} \quad (5)$$

where l is the path length of the sample. As described in Eq. (4), the screening factor was used to obtain the corrected rate constant for decay of furfuryl alcohol, $k_{\mathrm{obs,corr}}$. $k_{\mathrm{obs,corr}}$ was used to calculate the steady-state $^1O_2^*$ concentration by applying the second-order rate constant between furfuryl alcohol and $^1O_2^*$, $k_{^1O_2*,\mathrm{FFA}}$, according to Eq. (6).

$$[^1O_2^*]_{\mathrm{ss}} = \frac{k_{\mathrm{obs,corr}}}{k_{^1O_2^*,\mathrm{FFA}}} \quad (6)$$

2.3.4 $^1O_2^*$ quantum yield ($\Phi_{^1O_2^*}$)

The quantum yield expresses the efficiency of $^1O_2^*$ production, i.e., it is the fraction of absorbed photons that lead to $^1O_2^*$ production (Eq. 7).

$$\Phi_{^1O_2^*} = \frac{\#\text{ of } ^1O_2^* \text{ molecules formed}}{\#\text{ of photons absorbed}} \quad (7)$$

The quantum yield is particularly powerful for comparing $^1O_2^*$ production across different experimental setups (Ossola et al., 2021). For example, strong irradiation sources would produce larger absolute quantities of $^1O_2^*$ that are difficult to directly compare to weaker irradiation sources.

Considering the photophysical and chemical processes in the system, the $^1O_2^*$ quantum yield can be expressed in Eq. (8) (Sharpless, 2012; Schweitzer and Schmidt, 2003; Ossola et al., 2021):

$$\Phi_{^1O_2^*} = \Phi_{\mathrm{ISC}} \frac{k_{O_2}[O_2]}{k_d^T + k_{O_2}[O_2]} f_\Delta \quad (8)$$

where Φ_{ISC} is the fraction of excited singlet photosensitizer molecules that undergo intersystem crossing to the excited triplet state, k_d^T is the deactivation of triplets, k_{O_2} is the second-order rate constant for the physical quenching of $^3C^*$ with O_2, $\frac{k_{O_2}[O_2]}{k_d^T+k_{O_2}[O_2]}$ is the fraction of $^3C^*$ that is quenched by O_2, and f_Δ is the fraction of the quenching that leads to the formation of $^1O_2^*$.

In practice, two methods can be used to calculate $\Phi_{^1O_2^*}$. The direct method ($\Phi^{\mathrm{dir}}_{^1O_2^*}$), uses rate of light absorbance as well as a rate constant to account for the deactivation of $^1O_2^*$ in the solvent (Eq. 9).

$$\Phi^{\mathrm{dir}}_{^1O_2^*} = \frac{k_{\mathrm{obs,corr}} \cdot k_{\mathrm{d}}}{k_{^1O_2^*,\mathrm{FFA}} \cdot R_{\mathrm{abs}}} \quad (9)$$

where k_{d} is the deactivation of $^1O_2^*$ by water, $2.76 \times 10^5\ \mathrm{s}^{-1}$ (Appiani et al., 2017). The direct quantum yield depends on the rate of light absorbance, R_{abs}, which were determined using spectral irradiances determined using actinometry of either 2-nitrobenzaldehyde or p-nitroanisole/pyridine.

In contrast, the relative quantum yield of $^1O_2^*$, $\Phi^{\mathrm{r}}_{^1O_2^*}$, does not require photon flux to be quantitatively measured, and only normalizes rate of light absorbance of a compound of interest to a reference compound. In this study, perinapthenone (PN) was applied as reference compound. Perinaphthenone as a reference photosensitizer allows the normalization of the production of photooxidants and of the rate of absorbance for each experiment, due to possible slight changes in irradiation and/or experimental setup, since it has a well characterized $^1O_2^*$ quantum yield (Schmidt et al., 1994). Additionally, the triplet state of perinaphthenone does not react with furfuryl alcohol under typical experimental conditions (concentrations in the µM range), meaning that furfuryl alcohol loss reflects only reaction with singlet oxygen. This greatly simplifies $[^1O_2^*]_{\mathrm{SS}}$ and $\Phi_{^1O_2^*}$ calculations by enabling relative rate comparisons between singlet oxygen production and furfuryl alcohol consumption (Schmidt et al., 1994; Ossola et al., 2021). Finally, perinaphthenone possesses no acid-base functionality. Therefore, its triplet reactivity is not expected to exhibit a pH dependence, further supporting its use as a robust reference photosensitizer.

$$\Phi^{\mathrm{r}}_{^1O_2^*} = \frac{k_{\mathrm{obs,corr}}}{k_{\mathrm{obs,PN,corr}}} \frac{R_{\mathrm{abs,PN}}}{R_{\mathrm{abs}}} \Phi_{\mathrm{PN}} \quad (10)$$

In Eq. (10), $k_{\mathrm{obs,PN,corr}}$ is the observed decay of furfuryl alcohol due to $^1O_2^*$ produced by perinaphthenone that has been corrected for light screening, and $R_{\mathrm{abs,PN}}$ is the rate of light absorbance from the perinaphthenone sample.

2.4 Control experiments

2.4.1 Blank control

Control experiments were performed to isolate the reaction of furfuryl alcohol + $^1O_2^*$ and eliminate any other sources of furfuryl alcohol degradation. A blank control containing MilliQ water and 20 µM of furfuryl alcohol was irradiated to ensure the absence of probe decay due to impurities in the solvent (MilliQ water) or direct photodegradation of the chemical probe due to impurities. Based on the results of this control experiment, j_{FFA} in Eq. (2) was set to zero.

2.4.2 Dark control

A dark control solution was prepared for each set of photosensitizer experiments by adding a glass vial of sample solution covered with aluminum foil to protect the solution from irradiation. The dark control sample was conducted to account for any potential reactions between the photosensitizer and the probe in the absence of light.

2.4.3 Deoxygenated control (N_2 purge)

In order to investigate potential reactions of the triplet state of the photosensitizer with furfuryl alcohol, deoxygenation experiments were conducted. The borosilicate tube was sealed with a septum and bubbled with N_2 for 15 min to evacuate O_2 dissolved in solution and present in the headspace. Throughout the irradiation process, the time points were taken by adding a N_2 flow through the system, to maintain an inert environment. O_2 deoxygenation experiments were only conducted at the UBC laboratory. Since the same photosensitizer compounds were used, any triplet state reactivity with furfuryl alcohol observed, or lack thereof, is expected to be reproducible across all laboratories. Based on the results of the deoxygenation control experiments, we set the value of $k_{\mathrm{FFA}+{}^3\mathrm{C}^*}$ to zero in Eq. (2).

2.5 $^1O_2^*$ phosphorescence detection

To complement chemical probe quantification of $^1O_2^*$, we also used phosphorescence spectroscopy to directly detect the emission of $^1O_2^*$. Since $^1O_2^*$ is in a spin-forbidden state, its relaxation to the ground state can be detected as phosphorescence emission. Corresponding to an energy gap of 94 kJ mol^{-1} between the excited and ground states, this emission occurs in the near-infrared at a characteristic wavelength of 1270 nm. This distinct emission can be selectively filtered and monitored (Fig. S8). The instrumentation set up at the University of Calgary was a CryLas FTSS-355-Q3 Laser (532 and 355 nm emission options, 1000 Hz pulse rate), Spectral Products CM110 Monochromator (set to 1270 nm detection), and a Hamamatsu H10330A-45 photomultiplier tube (Fig. S8). A bi-exponential fit of the data is used to obtain information about the generation of $^1O_2^*$, and the preceding triplet excited state of the photosensitizer (Kabanov et al., 2019).

$$S(t) = S_0 \frac{\tau_\Delta}{\tau_\Delta - \tau_\mathrm{T}} \left(e^{\left(\frac{-t}{\tau_\Delta}\right)} - e^{\left(\frac{-t}{\tau_\mathrm{T}}\right)} \right) + Y_0 \tag{11}$$

Where $S(t)$ is the signal intensity at time t, S_0 is signal intensity at time 0, τ_Δ is the $^1O_2^*$ lifetime, τ_T is the photosensitizer triplet lifetime, and Y_0 is the baseline correction. In order to determine a quantum yield of $^1O_2^*$ for different photosensitizers, and using an excitation wavelength of 355 nm, we measured signal intensity as a function of absorbance for a reference photosensitizer (in this case perinaphthenone) and compared each photosensitizer to the reference. The response of intensity as a function of absorbance was determined for the reference photosensitizer, then the quantum yield of the other photosensitizers can be determined by the same method (Eq. 12).

$$\Phi_{^1O_2^*,\mathrm{sample}} = \frac{\mathrm{slope}_{\mathrm{sample}}}{\mathrm{slope}_{\mathrm{PN}}} \times \Phi_{^1O_2^*,\mathrm{PN}} \tag{12}$$

where slope is obtained as the linear regression of intensity response as a function of absorbance at the excitation wavelength. The standard error of the slope of the regression is reported as the uncertainty (Fig. S9). Phosphorescence measurements were conducted for five concentrations of each photosensitizing molecule dissolved in D_2O corresponding to absorbances of 0.1 to 0.5 AU. In addition to the photosensitizing molecules used for the photoreactor intercomparison study (Rose Bengal, perinaphthenone, lignin, and juglone), a suite of nitroaromatic molecules (2-nitroanisole, 3-nitroanisole, 4-nitroanisole, and 4-nitrophenol) were also tested.

2.6 Chemical actinometers

Two chemical actinometers, 2-nitrobenzaldehyde and *p*-nitroanisole/pyridine, were used to determine the absolute photon flux in the sample container in each setup. The decay of the chemical actinometer as a function of irradiation time was followed by (U)HPLC/UV detection to obtain the first-order rate constant, k_{obs}. The measured irradiance spectrum of the light source, $I_{\lambda,\mathrm{meas}}$, was used to calculate a relative irradiance spectrum, $I_{\lambda,\mathrm{rel}}$, according to Eq. (13).

$$I_{\lambda,\mathrm{rel}} = \frac{I_{\lambda,\mathrm{meas}}}{\sum I_{\lambda,\mathrm{meas}}} \tag{13}$$

With the relative irradiance spectrum, a scaling factor, γ, was calculated as described by Ossola et al. (2021) (Eq. 14):

$$\gamma = \frac{k_{\mathrm{obs}}[\mathrm{comp}]_0 l}{\Phi_{\mathrm{comp}} \sum I_{\lambda,\mathrm{rel}} \left(1 - 10^{-\varepsilon_\lambda [\mathrm{comp}]_0 l}\right) \Delta\lambda} \tag{14}$$

where $[\mathrm{comp}]_0$ was the concentration of the compound at the start of the irradiation, l is the path length of the light, Φ_{comp} is the quantum yield of the compound, ε_λ is the extinction coefficient of the compound, and $\Delta\lambda$ is the wavelength increment (typically 1 nm). For *p*-nitroanisole the quantum yield was calculated by: $\Phi_{\mathrm{PNA}} = 0.29[\mathrm{Pyr}] + 2.9 \times 10^{-4}$ (Laszakovits et al., 2017), where [Pyr] is the concentration of pyridine used. For 2-nitrobenzaldehyde, $\Phi_{\mathrm{2NB}} = 0.41 \pm 0.02$

(Galbavy et al., 2010). Both chemical actinometer quantum yields are reported to be independent of wavelength.

The scaling factor was used to scale the relative irradiance to obtain absolute irradiance ($I_{\lambda,0}$) (Ossola et al., 2021), as shown in Eq. (15).

$$I_{\lambda,0} = I_{\lambda,rel} \cdot \gamma \tag{15}$$

Absolute irradiance was then used to calculate a rate of light absorbance for each of the photosensitizing molecules for each photoreactor. Absolute irradiance was also used to compare photoreactor light output to simulated sunlight conditions.

2.7 Comparison to atmospheric sunlight

The NCAR Tropospheric Ultraviolet and Visible (TUV) Radiation Model was used to simulate sunlight at solar noon for the summer solstice of 2025 in Vancouver (49.2827° N, 123.1207° W), Canada (20 June, 13:14 local time) (https://www.acom.ucar.edu/Models/TUV/Interactive_TUV/, last access: 29 July 2025). The measurement altitude was 5 km to represent the mid-troposphere, and total irradiation was considered. Surface albedo was set to 0.1, overhead ozone column concentration was set to 300 du, cloud optical depth was set to 0, and aerosol optical depth was set to 0.235. Conversion factors to equivalent hours of sunlight for atmospherically relevant photosensitizers were calculated according to Eq. (16).

$$\text{Conversion Factor} = \frac{R_{\text{abs}}}{R_{\text{abs,sunlight}}} \tag{16}$$

2.8 Wavelength dependent quantum yield experiments

To test the wavelength dependence of $^1O_2^*$ quantum yields of lignin and juglone, wavelength dependent experiments were performed at UCD. The illumination experiments were performed with a 1000 W mercury-xenon arc lamp with a downstream monochromator (Spectral Energy) and a 310 nm longpass filter. The illumination chamber was temperature controlled with a water bath set to 25 °C. Samples were illuminated with 313, 334, and 366 nm light. Experiments were performed in 1 cm Spectrocil quartz cells (Starna Cells, 1-Q-10-GL14-C) with a plastic cap. The cuvettes initially held 3 mL of sample, and at each illumination time point, 90 µL of solution was removed to perform HPLC-PDA analysis of FFA. At each wavelength, we determined the $^1O_2^*$ quantum yield of lignin and juglone by illuminating solutions of 20 mg L^{-1} lignin and 20 µM FFA, and 20 µM juglone and 20 µM FFA, respectively. At each wavelength, actinometry was quantified by illuminating 10 µM 2NB. The $^1O_2^*$ quantum yields were calculated using the direct method with 2NB actinometry following Eq. (9).

3 Results

3.1 Intercomparison of photoreactor experimental set ups

3.1.1 Light types

Intercomparing photoreactor light sources is essential for evaluating the reproducibility and the atmospheric relevance of $^1O_2^*$ measurements across different laboratory setups, because light absorption by chromophoric organic matter is the first step in the formation of $^1O_2^*$. We compared xenon lamps as solar simulator systems at UCD (Heinlein et al., 2025) and at Ircelyon (Petersen-Sonn et al., 2025), as well as two configurations of 16 bulbs of broad-band UV lights in a commercial Rayonet photoreactor at UBC (Borduas-Dedekind et al., 2024) (Fig. 2, Table 1).

These choice of light source has advantages and disadvantages to consider. Xenon lamps produce a broad spectrum most similar to the solar spectrum, including the photochemically active UV range (280–400 nm). Xenon lamp photoreactors provide a better mimic of natural sunlight, but may be less suited for mechanistic, wavelength-specific experiments. In contrast, UV-centred bulbs enable selective irradiation in higher-energy UV regions, but fail to replicate the full spectral profile of solar irradiance (Sect. 3.2, Fig. 3b).

Although this intercomparison focuses on these four systems, many other photoreactors are also used in the community. Examples reported in recent atmospheric photochemistry studies include multiple 300 W xenon lamps (Go et al., 2022, 2024; Liu et al., 2025), custom LED reactors equipped with discrete monochromatic LEDs (Wu et al., 2021; Lee et al., 2025; Vallon et al., 2022), and additional photoreactors with different power xenon-lamp sources. In Sect. 3.2.4, we quantify each photoreactors light source compared to natural sunlight, and in Sect. 3.3.8 we assess the potential wavelength dependence of $^1O_2^*$ formation. Together, these comparisons provide the foundation for interpreting interlaboratory differences in $^1O_2^*$ production, while recognizing the broader diversity of photoreactor setups used across the community.

3.1.2 Number of samples per experiment

The number of samples that can be irradiated simultaneously depends on the light setup (Fig. 2, Table 1, column 4). If the setup has one point source, such as a xenon lamp, then only one sample can be irradiated at at time (Figs. 2b, c and S6). On the other hand, if the setup has multiple bulbs arranged in an array, like a Rayonet or an incubator, then dozens of samples can be irradiated simultaneously. These multi-bulb setups can have a carousel, like the setup at UBC (Fig. S4), or have rotating lights (Fig. 2a). Multiple lights provide the advantage of increasing the experimental throughput. Additionally, chemical actinometry methods that were exposed to

Table 1. Photoreactor details for each laboratory. Light sources, temperature ranges, operational temperature used for this study, # of samples that can be irradiated simultaneously, and sample volumes.

Lab	Light Source	Temperature Control Range (°C)	Operational Temperature (°C)	# of Samples	Sample Volume (mL)
UBC	UVA, UVB, & Fluorescent	20–34	22	16	5
UCD	Xenon	0–50	20	1	1–20
Ircelyon	Xenon	0–50	20	1	20

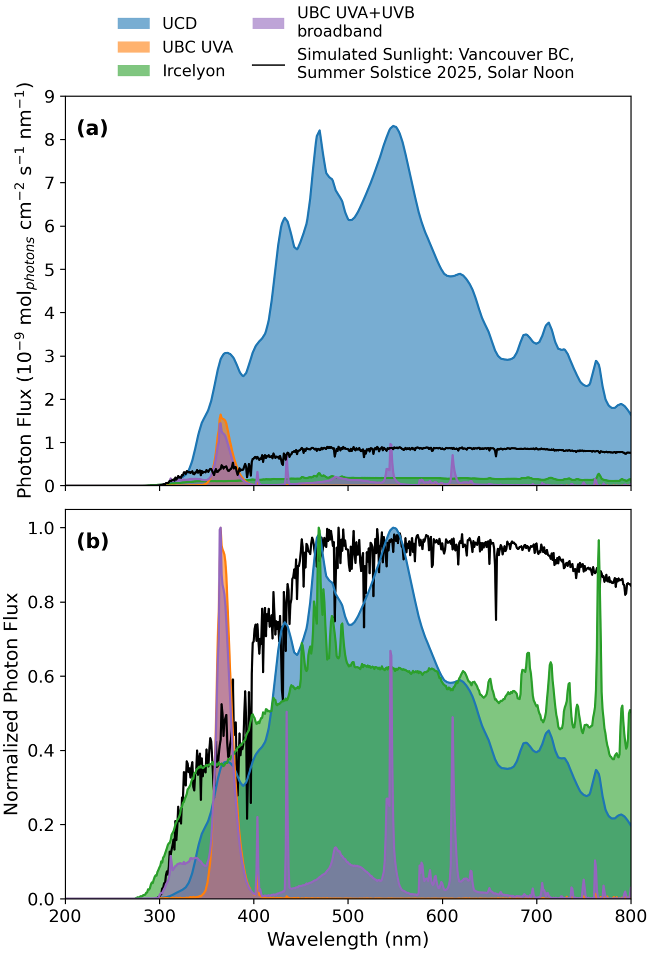

Figure 3. Irradiance measurement of photoreactor setups, showing **(a)** Photon flux quantified using 2-nitrobenzaldehyde actinometry ($\mathrm{mol_{photons}\,cm^{-2}\,s^{-1}\,nm^{-1}}$, average of triplicate actinometry experiments) and **(b)** normalized to peak irradiance. UCD is shown in blue, Ircelyon in green, and UBC in orange (UVA only) and purple (UVA+UVB broadband). Sunlight was simulated from the NCAR quick TUV calculator (https://www.acom.ucar.edu/Models/TUV/Interactive_TUV/) for solar noon on the summer solstice of 2025 in Vancouver, British Columbia (see Sect. 3.2.4 for model details).

the exact same irradiation conditions were expected to provide the most accurate photon flux measurements, which is only possible when multiple samples can be irradiated simultaneously.

3.1.3 Temperature control

All three photoreactors can control sample temperature, which is important for chemical kinetic experiments, including for the reaction of $^1O_2^*$ with its furfuryl alcohol probe. Indeed, Appiani et al. (2017) calculates a +2 % increase in rate constant per °C increase in temperature. The Rayonet temperature at UBC is measured using a thermal couple probe and is regulated using a perforated copper coil inside the photoreactor where liquid nitrogen flows through a needle valve (Fig. S4). However, this setup does not benefit from the same accuracy or temperature range that the water-cooled temperature regulators provide in the Ircelyon and UCD photoreactors (20–34 °C for the liquid nitrogen cooling system vs. 0–50 °C for water bath cooling systems, Table 1). Operational temperatures used for intercomparison experiments in this work were 22 °C at UBC and 20 °C at Ircelyon and UCD (Table 1, column 3).

3.2 Measuring irradiance

3.2.1 Comparing chemical actinometers

Chemical actinometry allows for the quantification of the photon flux from an irradiation source, necessary to intercompare photochemical results across samples, setups and studies. Chemical actinometers are compounds with well characterized direct photolysis chemistry and with known quantum yields and absorption cross sections. For our intercomparison, we used two chemical actinometers: 2-nitrobenzaldehyde (Galbavy et al., 2010) and p-nitroanisole/pyridine (Laszakovits et al., 2017). Molar absorption coefficients for both compounds define the wavelength ranges over which they can be used as chemical actinometers, i.e., their validity ranges (Fig. S10). The validity ranges for the p-nitroanisole/pyridine system and for 2-nitrobenzaldehyde are 300–400 nm (Laszakovits et al., 2017), and 280–400 nm (Galbavy et al., 2010), respectively. For these actinometers to be effective, these ranges should overlap with the emission spectra of the photoreactor, which is the case for our intercomparison (Sect. 3.1). Additionally, both chemical actinometers should be used at low optical depth, and potential light screening by all chromophores, including reaction products, should be considered.

The p-nitroanisole (PNA) and pyridine (Pyr) actinometery pair has the advantage that the time decay can be adjusted from min to h (depending on the strength of the light source) by varying the pyridine concentration (i.e $\Phi_{\mathrm{PNA}} = 0.29[\mathrm{Pyr}] + 2.9 \times 10^{-4}$). For example, if the sample's furfuryl alcohol decay takes 12 h, the concentration of Pyr can be tuned to match the timeline of the probe kinetics. In contrast, the quantum yield of the 2-nitrobenzaldehyde system is fixed ($\Phi_{\mathrm{2NB}} = 0.41 \pm 0.02$) and cannot be tuned to match the timescale of $^1O_2^*$ probe decay experiments. For these reasons, when an experiment may be subject to varying photon flux over the irradiation period (for example, in natural sunlight experiments when the angle of the sunlight changes throughout the day), the p-nitroanisole/pyridine actinometer is preferred due to its tunable quantum yield. However, in the context of lab-based photoreactors, we found that 2-nitrobenzaldehyde was operationally simpler to use. If photon flux is expected to remain stable throughout a $^1O_2^*$ probe experiment, the 2-nitrobenzaldehyde actinometer may be the more suitable option.

To demonstrate that these two chemical actinometers work interchangeably, we compared them across setups. As expected, they provided nearly identical photon fluxes as a function of wavelength for the same photoreactor (Fig. S11). Consequently, the rate of light absorbance of each photosensitizer in different photoreactor configurations did not differ by more than 11 % when using both chemical actinometers (Table S5). Nevertheless, we recommend conducting illumination experiments with both 2-nitrobenzaldehyde (Galbavy et al., 2010) and p-nitroanisole/pyridine (Laszakovits et al., 2017) chemical actinometers at the start of a study, since the reproducibility of the photon fluxes determined by two independent actinometers provides confidence that the photon flux is accurately calculated. When the agreement is established, subsequent experiments may rely on a single actinometer.

3.2.2 Photoreactor photon flux

To compare the absolute and normalized photon fluxes from each setup, we measured their spectrally resolved irradiance profiles using a spectrophotometer. Absolute irradiance was calculated by combining the irradiance profiles with 2-nitrobenzaldehyde actinometry, following Eqs. (13)–(15). As a standard reference, we integrated the photon flux over 200–800 nm, noting that wavelengths below 290 nm contribute negligibly to tropospheric irradiance whereas wavelengths above approximately 600 nm are unlikely to initiate photochemistry. The UCD photoreactor, with a 1000 W xenon light source, had the highest absolute photon flux, with an integrated irradiance in the 200–800 nm wavelength range of 4686 W m^{-2} (Fig. 3a). The Ircelyon photoreactor, with a 150 W xenon lamp, had a lower integrated irradiance at 171 W m^{-2}. The UBC photoreactor had an integrated irradiance of 103 W m^{-2} for the UVA configuration, and 163 W m^{-2} for the UVA+UVB broadband configuration. The Tropospheric Ultraviolet and Visible (TUV) radiation modelled sunlight for the 2025 summer solstice in Vancouver, BC, was 774 W m^{-2} over 200–800 nm. This modeled sunlight value is higher than those of the UBC and Ircelyon photoreactors, but lower than the UCD photoreactor, hence the need to quantify the approximate sunlight equivalents for each photoreactor (Sect. 3.2.4).

Calculating absolute irradiance required combining the spectrophotometer measurements of relative photon fluxes as a function of wavelength with chemical actinometry. UCD found significant variability in the relative photon fluxes for measurements made on the same day but with different optical probe positions in the sample chamber (see Sect. S12). We believe that this variability was due to internal reflections within the UCD illumination chamber. To determine the most correct relative photon fluxes, we used experiments to determine the $^1O_2^*$ quantum yield from perinaphthenone to constrain the 548 nm / 347 nm intensity ratio, which we used as a marker of the photon fluxes at long and short wavelengths (Sect. S12 and Fig. S21 in the Supplement). The combination of actinometry (to get the short-wavelength region) and a reference photosensitizer (to characterize the long-wavelength region) allowed us to constrain the UCD photon flux by identifying the influence of internal reflections on the spectral shape. By testing if experiments with two actinometers yielded equivalent photon fluxes, and by ensuring that experiments with reference photosensitizers yielded published values, this tested the photon flux across a wide range of wavelengths. This highlights the utility of actinometry and model photosensitizers as robust tools to constrain the photon flux in an experimental illumination system.

3.2.3 Spectral range of wavelengths

The spectral range of wavelengths and their peak intensity are also important considerations for interpreting photochemical results. The Ircelyon photoreactor has light that extends to 285 nm, a lower threshold than the simulated sunlight from the TUV model (Fig. 3b). The UBC photoreactor configurations had UVA bulbs (348–405 nm), and UVA+UVB bulbs (300–405 nm), with some additional irradiance at longer wavelengths due to fluorescence from the UVB bulbs. The UBC spectral profiles differed from the broad distribution of natural sunlight, with implications for extrapolating to the real atmosphere (Fig. 3b). Normalized photon fluxes showed similar spectral shapes for the xenon lamp setups at UCD and Ircelyon (Fig. 3b), suggesting consistency in the emission characteristics despite differences in absolute intensity. Based on differences in spectral range of the different light sources, we also explored the possible quantum yield dependence on wavelength in Sect. 3.3.8.

Table 2. Rate of light absorbance equivalent hours of sunlight for photosensitizers with atmospherically relevant moieties for an hour in each photoreactor setup calculated according to Eq. (16). Rates of light absorbance for photoreactors were calculated from 2-nitrobenzaldehyde actinometry and are the mean value of triplicate experiments.

Sensitizer	Light absorbance equivalent hours (h)			
	UBC UVA	UBC UVA+UVB broadband	UCD	Ircelyon
Perinaphthenone	0.72	0.67	6.3	0.26
Lignin	0.45	0.60	5.0	0.29
Juglone	0.23	0.29	7.1	0.24

3.2.4 Rate of light absorbance equivalent hours of sunlight

To estimate the equivalent hours of sunlight experiences by the samples in each photoreactor, we compared rates of light absorbance by photosensitizers in each four photoreactor configurations to conditions under natural sunlight. The conversion factor, calculated using Eq. (16), represents the number of hours of solar exposure at 5 km altitude over Vancouver, Canada (a representative mid-tropospheric location), required to match 1 h of irradiation in a given photoreactor.

Equivalent hours of sunlight were determined for perinaphthenone, lignin, and juglone, based on rates of light absorbance from 2-nitrobenzaldehyde actinometry (Table 2). Consistent with our observed photon fluxes (Sect. 3.2.2), the UCD photoreactor had the highest effective light intensity with conversion factors of 5.0 to 7.1 (Table 2). In contrast, the Ircelyon photoreactor yielded the lowest values, with less than 0.3 h of natural sunlight for each hour in the photoreactor, consistent with a weaker irradiance. The UBC photoreactor setups had intermediate conversion factors, ranging from 0.23 to 0.72. These trends reflect differences in both total irradiance and spectral overlap with the absorbance features of the photosensitizers, highlighting the need to characterize and report spectral irradiance, light intensity, and action spectra of light absorbance for each illumination system.

3.3 Quantifying $^1O_2^*$ Production

3.3.1 Measuring $^1O_2^*$ using furfuryl alcohol as a probe

Furfuryl alcohol is widely used as a chemical probe for $^1O_2^*$ due to its well characterized and selective reactivity (Haag et al., 1984; Appiani et al., 2017). Recent work has expanded the family of furan-based probes. For example, Arciva et al. (2025) reported singlet oxygen reaction kinetics for 17 furan derivatives, highlighting that alternative probes may be selected for specific experimental constraints. For example, less volatile probes such as 2-methylfuran-3,4-dicarboxylic acid may be advantageous in open systems where volatility is a concern, although this was not an issue for the capped solutions used here. To the best of our knowledge, chemical compatibility has not been systematically explored as a limitation of FFA as a probe for $^1O_2^*$.

To accurately quantify $^1O_2^*$ production, furfuryl alcohol must display pseudo-first order kinetics as a function of irradiation time (Figs. S2–S7). This linearity is necessary, as a deviation indicates that $^1O_2^*$ is no longer under steady-state conditions and other sources and sinks of $^1O_2^*$ are likely contributing to furfuryl alcohol's decay. Furthermore, deviations from pseudo-first-order kinetics can also be observed for longer irradiation times and weak light sources. To account for these deviations, we have previously suggested removing furfuryl alcohol time points resulting in a change in slope greater than 25 % (Borduas-Dedekind et al., 2024).

When using a chemical probe to determine $^1O_2^*$, all possible sinks of the probe need to be considered and accounted for. These sinks include photolysis, light screening, reactivity with other oxidants such as •OH, and reactivity with other molecules and excited state photosensitizers (see Sect. 3.3.2). For example, a dark control will confirm the lack of reactivity between the photosensitizer and the probe in the absence of light (Fig. S1). Additionally, correcting observed decays of the probe for light screening according to Eq. (4) is necessary to account for any heterogeneity of chromophores in the sample and particularly due to concentrated and coloured samples. In our case, the screening factors were optimized to be close to 1, by reducing sample absorbance, to specifically avoid screening (Tables S1–S4). However, in the Ircelyon photoreactor, the 3.5 cm irradiation pathlength through the sample produced screening factors that deviated from 1. Furthermore, to account for •OH reactivity with furfuryl alcohol, we recommend adding an •OH quencher such as isopropanol to the solution (Bogler et al., 2022; Borduas-Dedekind et al., 2024). Alternatively, •OH can be quantified explicitly with a probe such as benzoic acid (Klein et al., 1975) or terephthalic acid (Manfrin et al., 2019). Manfrin et al. (2019) found that •OH accounted for up to 32 % of the observed furfuryl alcohol loss under 311 nm irradiation, but only up to 2 % under 365 nm irradiation, highlighting the importance of quenching •OH or accounting for probe loss from •OH in the presence of UVB light.

Yellow impurities in furfuryl alcohol can also influence the reaction kinetics and the absorbance of the sample in the UVA region (Fig. S12). These impurities can contribute to the direct photodegradation of furfuryl alcohol by 3.1 %, as shown in Fig. S13 (Marchisio et al., 2015; Maizel et al., 2017). To limit this issue, stock solutions should be stored at 4 °C, and in dark environments (Ossola et al., 2021). Overall, using a probe such as furfuryl alcohol is an indirect method of quantification but does lend itself readily to high throughput experiments of atmospheric sample extracts.

3.3.2 Control experiments for $^3C^*$ reacting with furfuryl alcohol

Removing oxygen by bubbling with N_2 from sample solutions is an important control for verifying that the $^3C^*$ of the photosensitizer did not react with furfuryl alcohol at a competitive rate, which is the case for the the photosensitizing molecules used in our photoreactor intercomparison (Figs. S2, S3). However, we found that excited states of atmospherically relevant nitroanisoles (Xu et al., 2022), can react with furfuryl alcohol in the absence of O_2 leading to a $^1O_2^*$ false positive (Fig. S14). Nitrogen-containing compounds are ubiquitous in organic aerosols and have been found in wildfire smoke and $PM_{2.5}$ filters (Xu et al., 2018; Li et al., 2025b; Zheng et al., 2023; Fleming et al., 2020), highlighting the importance of conducting this control experiment for the atmospheric context.

Furthermore, previous studies have used the kinetic solvent isotope effect as a diagnostic tool to assess the decay of furfuryl alcohol from oxidants other than $^1O_2^*$ (Davis et al., 2018; Lyu et al., 2023). The kinetic solvent isotope effect relies on the difference in the deactivation lifetime of $^1O_2^*$ in H_2O (3.5 µs; Bregnhøj et al., 2016) and in D_2O (67 µs; Nonell and Flors, 2016). Although not conducted in our intercomparison study, kinetic solvent isotope effect experiments can be a useful diagnostic tool to quantify the furfuryl alcohol from oxidants other than $^1O_2^*$.

3.3.3 Calculation of quantum yields via absolute and relative methods

There are two approaches to calculate a quantum yield. There is an absolute method, $\Phi^{\mathrm{dir}}_{^1O_2^*}$, which relies on chemical actinometry and is measured for instance by 2-nitrobenzaldehyde or p-nitroanisole/pyridine according to Eq. (9) and used to generate Fig. 4c. In addition, there is a relative method, $\Phi^{\mathrm{r}}_{^1O_2^*}$, which uses a reference photosensitizer such as perinaphthenone along with Eq. (10). This method requires that a solution of perinaphthenone be run side by side with the samples in a multi-sample holder and captures changes in photon flux throughout the irradiation experiment.

For this intercomparison study, we ran both sets of experiments to evaluate the differences between the absolute and relative methods. Values between the two methods ($\Phi^{\mathrm{dir}}_{^1O_2^*}$ vs. $\Phi^{\mathrm{r}}_{^1O_2^*}$) were consistently within 15 % of each other for all sensitizers, and we thereby suggest 15 % as a reasonable metric for acceptable agreement between quantification methods (Tables S1–S4). Agreement between these methods is expected and supports the stability of the lights sources in all four experimental setups (Table S5). Chemical actinometry has the advantage of providing both the photon flux and the corresponding quantum yield (Eq. 9), while the relative method only provides quantum yields (Eq. 10). Applying both approaches at the onset of a study can provide a consistency check to identify systematic biases in the light distribution and actinometry based quantification within the photoreactor. Nevertheless, previous aqueous environmental studies of $^1O_2^*$ have favoured the use of actinometry over reference photosensitizer to quantify $^1O_2^*$ quantum yields (24 studies to 4 studies, reported by Ossola et al., 2021).

3.3.4 $^1O_2^*$ Quantum Yield from the probe method

Rates of light absorbance and $^1O_2^*$ steady-state concentrations differed by several orders of magnitude across the different laboratories (Fig. 3). These differences reflect variation in photon flux among the light sources, with higher intensity sources producing higher absorbance rates and correspondingly higher $^1O_2^*$ concentrations (Fig. 4a, b). Despite these order of magnitude differences in R_{abs} and $[^1O_2^*]_{\mathrm{SS}}$, the apparent quantum yield, $\Phi_{^1O_2^*}$, for Rose Bengal and for perinaphthenone were consistent and reproducible across photoreactors and aligned with literature values (Schmidt et al., 1994; Wilkinson et al., 1993) (Fig. 4c), indicating that these sensitizers singlet oxygen generation efficiency exhibit minimal dependence on the irradiation conditions explored here.

In contrast, lignin and juglone exhibited deviations in quantum yields across photoreactors. Specifically, xenon lamp systems (UCD and Ircelyon) yielded lower $\Phi_{^1O_2^*}$ values, whereas the UV bulb system (UBC) produced higher values. For juglone, this discrepancy was particularly pronounced, as the highest photon flux (UCD; Fig. 4a) corresponded to the lowest measured quantum yield (Fig. 4c, left). These results suggest that, unlike Rose Bengal and perinaphthenone, the apparent quantum yields of lignin and juglone are influenced by the spectral distribution of the light source, consistent with a wavelength dependent mechanism.

3.3.5 Wavelength-dependency of quantum yields

$^1O_2^*$ quantum yields have been observed to decrease as a function of wavelength in surface water samples (Partanen et al., 2020) and in juglone aqueous solutions (Manfrin et al., 2019). In this study, we observed similar trends for two samples specifically: lignin and juglone. Indeed, shorter wavelengths led to an increase in $\Phi_{^1O_2^*}$ (Figs. 4, S20). This wavelength dependency may be due to higher energy photons leading to higher singlet to triplet intersystem crossing rates, k_{ISC}.(Drozd et al., 2024) This increase in intersystem crossing rate has been observed for a range of aromatic molecules relevant to the atmosphere (Valiev et al., 2025). While a quantitative relationship between photon energy and increasing $\Phi_{^1O_2^*}$ does not yet exist, there is clear evidence for wavelength-dependent quantum yields of photosensitizing molecules within chromophoric dissolved organic matter,(Partanen et al., 2021), and we now extend this observation to atmospherically relevant molecules like lignin and juglone. For inter-comparing $\Phi_{^1O_2^*}$, it is thus necessary to report the irradiance spectrum and if possible use different light

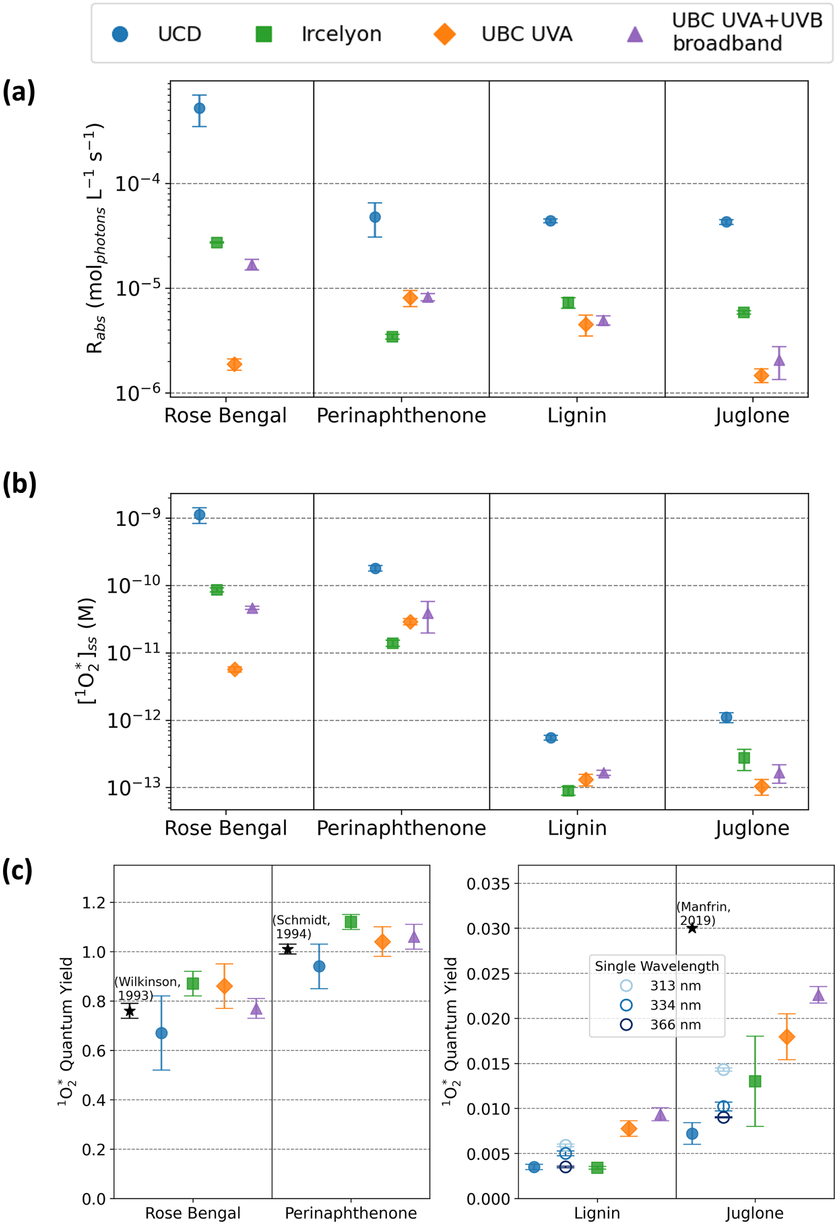

Figure 4. $^1O_2^*$ formation parameters for each photosensitizer and photoreactor setup. Panel **(a)** is the rate of light absorbance for each photosensitizing molecule in each photoreactor setup in (mol$_{\text{photons}}$ L^{-1} s^{-1}) (log scale), panel **(b)** is $^1O_2^*$ steady-state concentrations (M) (log scale), and **(c)** is the resulting $^1O_2^*$ quantum yield values, calculated using Eq. (9), separated into efficient photosensitizers (Rose Bengal and perinaphthenone, left panel) and less efficient photosensitizers (juglone and lignin, right panel), with adjusted *y*-axes. Previously reported values, when available, are plotted as black stars. Previously reported quantum yield values in water are 0.76 ± 0.02 for Rose Bengal (Wilkinson et al., 1993), 1.01 ± 0.03 (Schmidt et al., 1994) for perinaphthenone, and 0.03 for juglone (excitation wavelength centred at 365 nm) (Manfrin et al., 2019). Single wavelength experiments to test for the wavelength dependence of $\Phi_{^1O_2^*}$ (Sect. 2.8) for lignin and juglone are shown as open circles (conducted at 313, 334, and 366 nm).

sources for the interpretation of $\Phi_{^1O_2^*}$ values. This wavelength sensitivity may introduce a measurement-dependent bias when different light sources are used and should therefore be treated as a methodological constraint.

Due to wavelength dependencies, results obtained using narrow or single wavelength irradiation can be difficult to reliably extrapolate to the broader solar spectrum. Accordingly, using sunlight-mimicking irradiation sources, or combinations of several narrow band excitations are best recommended. In fact, Anton et al. (2024) recommended that, to obtain more accurate measurements, researchers should: (1) select a chemical actinometer that absorbs light in the same

Table 3. $^1O_2^*$ quantum yields ($\Phi_{^1O_2^*}$) calculated from Eq. (10) for photosensitizers: Rose Bengal, Lignin, Juglone, 2-nitroanisole, 3-nitroanisole, 4-nitroanisole, and 4-nitrophenol, measured by chemical probe (FFA) and direct phosphorescence (1270 nm).

Sensitizer	Chemical Probe (UBC UVA) ($\Phi_{^1O_2^*}$, %)	Direct Phosphorescence (1270 nm) ($\Phi_{^1O_2^*}$, %)
Rose Bengal	83 ± 10	78.1 ± 10.0
Lignin	0.75 ± 0.07	0
Juglone	1.73 ± 0.22	5.3 ± 1.7
2-nitroanisole	1.25 ± 0.18	0
3-nitroanisole	34.4 ± 2.1	24.3 ± 4.8
4-nitroanisole	8.83 ± 1.07	0
4-nitrophenol	0.80 ± 0.01	0

spectral region as the compound of interest, and (2) minimize inner filter effects by employing optically transparent solutions.

3.3.6 $^1O_2^*$ quantum yield from phosphorescence data

We conducted phosphorescence measurements of $^1O_2^*$ as a direct spectroscopic technique to further intercompare reported $\Phi_{^1O_2^*}$ values measured using a chemical probe. All four sensitizers, as well as nitrophenol and nitroanisoles as additional sensitizers relevant for BrC, were excited at 355 nm and the relaxation of $^1O_2^*$ to the ground state was detected at 1270 nm (Kabanov et al., 2019). The $\Phi_{^1O_2^*}$ values between the two methods only matched well for the reference sensitizer Rose Bengal (Table 3).

Interestingly, lignin, 2-nitroanisole, 4-nitroanisole and 4-nitrophenol had $^1O_2^*$ quantum yields of 0 in the phosphorescence set up, but measurable $^1O_2^*$ quantum yields using the chemical probe method (Table 3). We hypothesize that this discrepancy is due to the detection limit of the photomultiplier tube in the phosphorescence set up. To further test this hypothesis, we used a range of concentrations of the sensitizers (absorbance 0.1–0.5), yet $^1O_2^*$ signals remained undetectable. We did not test the role of oxygen saturation to maintain comparability with the ambient-air conditions of the chemical probe experiments.The differences observed among the photosensitizers support the conclusion that the direct phosphorescence method, despite its high specificity, may lack sufficient sensitivity to detect $^1O_2^*$ emission for photosensitizers with low $^1O_2^*$ quantum yields.

For juglone, a phosphorescence signal was detected, and the $^1O_2^*$ quantum yield obtained was three times higher than with the chemical probe method (Table 3). This discrepancy is hypothesized to be due to an observed wavelength dependence on $^1O_2^*$ quantum yield from the single wavelength laser used (355 nm) in phosphorescence experiments (Sect. 3.3.4).

The relatively high quantum yield for 3-nitroanisole by both methods compared to 4- and 2-nitroanisole (Table 3) may be explained by the unique meta position of the methoxy and the nitro substituents. Indeed, the meta position has been suggested to lead to an excited state through a low lying π,π^* triplet state (Mir et al., 1998), consistent with a high $^1O_2^*$ quantum yield (Schweitzer et al., 2003; Gollnick et al., 1970). Furthermore, a quantum yield of 8.83 % was measured for 4-nitroanisole using the chemical probe method, however no corresponding signal was detected via direct phosphorescence. We hypothesize that this discrepancy can be attributed to the reactivity of the $^3C^*$ of the this nitroanisole with furfuryl alcohol observed in the absence of O_2 (Sect. 3.3.1, Fig. S14). The proposed mechanism is a substitution reaction involving the nitro group on nitroanisole and and the alcohol on furfuryl alcohol, proceeding under light with wavelengths greater than 300 nm in water (Dulin and Mill, 1982). In these cases, furfuryl alcohol is not a suitable probe for $^1O_2^*$ in the presence of nitro groups, which are particularly prevalent in BrC and the atmospheric chemistry context.

Phosphorescence measurements can be used to diagnose whether quenching of $^1O_2^*$ is significant in complex samples (Madhiyan and Moor, 2026). Although not conducted here due to the use of single molecule sensitizers, $^1O_2^*$ can be generated using a known sensitizer at a wavelength outside the absorbance range of the sample matrix and the phosphorescence signal at 1270 nm compared in the presence and absence of the sample. A reduction in the signal when the sample is present indicates additional quenching of $^1O_2^*$ and this approach is complementary to chemical probe methods. For example, in systems that do not absorb above 500 nm, Rose Bengal can be excited at 550 nm to generate $^1O_2^*$ and evaluate quenching by the sample matrix.

Overall, the direct phosphorescence method and the indirect probe method remain complimentary. The phosphorescence technique does not suffer from the interferences outlined for the indirect probe method since it tracks $^1O_2^*$ directly (Sect. 3.3.1 and 3.3.2). However, it does not provide information on $^1O_2^*$ reactivity (i.e. no information on k_{obs} that chemical probe methods provide (Partanen et al., 2020; Schweitzer and Schmidt, 2003).

3.3.7 Role of dissolved oxygen

Discrepancies between phosphorescence and chemical probe methods may also be attributed to differences in dissolved O_2 (Eq. 8). To test this hypothesis, we estimated the partial pressure of O_2 at the location of the measurement, used O_2's Henry's Law constant to estimate the amount of dissolved O_2 and then calculated the fraction of triplets quenched by O_2 using the constant for the deactivation triplets, k_d^T from Erickson et al. (2018) and calculating ($k_{O_2}[O_2]$) (see additional details in the Supplement). The calculation of $[O_2]$ in solution led to calculated $^3C^*$ deactivation pathways yields, $k_{O_2}[O_2]$, that were 2.8 times larger than k_d^T in Vancouver, and 2.5 times larger in Calgary. In other words, a lower p_{O_2} results in a lower $\Phi_{^1O_2^*}$, according to Eq. (8), consistent with the quantum yield for Rose Bengal that we reported in Table 3.

3.3.8 Photochemical action regions of light absorbance

Photochemical action spectra of light absorbance represent rates of light absorbance as a function of wavelength, and provide insights into the specific wavelength regions that drive photochemical reactions. Rose Bengal exhibited a strong absorbance peak at 549 nm in water, which dominated its photochemical action spectra of light absorbance in all photoreactors except the UBC UVA setup, where no irradiance was present at this wavelength (Fig. 5a). Remarkably, despite this difference, $\Phi_{^1O_2^*,\mathrm{RB}}$ remained comparable across all setups, indicating no wavelength dependence. Perinaphthenone action regions of light absorbance also differed, with xenon lamp photoreactors displaying broader regions (e.g 294–480 nm at Ircelyon) and narrower regions in the UV photoreactor setups (e.g 348–405 nm for UBC UVA) (Fig. 5b). The differences in action regions of light absorbance did not lead to an observed difference in $\Phi_{^1O_2^*,\mathrm{PN}}$, suggesting that the quantum yield is independent of wavelength, and effectively normalizes R_{abs} and $^1O_2^*$ production.

The juglone action spectra of light absorbance peaked at longer wavelengths in xenon lamps (433 nm at UCD, 421 nm at Ircelyon), where lower $\Phi_{^1O_2^*,\mathrm{Juglone}}$ values were observed (Fig. 4c). UBC photoreactors showed peaks at 365 nm, with the UVA+UVB broadband setup extending further into the UV (down to 304 nm) and producing the highest $\Phi_{^1O_2^*,\mathrm{Juglone}}$, consistent with increased excitation by higher energy photons (Fig. 5d). A similar trend was observed for lignin; increased contributions from high energy photons in the UBC UVA and UVA+UVB broadband systems led to higher $\Phi_{^1O_2^*,\mathrm{Lignin}}$ compared to the UCD and Ircelyon xenon lamp setups. This general trend is consistent with previous studies for quantum yields of photodegradation (Anton et al., 2024).

An important consideration in the analysis of photochemical action regions of light absorbance is the potential for light scattering in absorbance measurements. Light scattering should be considered a source of uncertainty in UV–Vis absorbance measurements, even in filtered samples, as particles smaller than filter pore size (0.22 µm here) can still contribute to scattering and filtration alone will not necessarily eliminate this effect. Dissolved organic matter can form colloidal structures or aggregates smaller than the filter pore size, which remain in solution and can scatter light. The formation and optical properties of these colloids depend on the composition and source of the organic matter, and thus filtration does not guarantee the removal of all scattering effects (Sect. S8, Figs. S15, S16) (Bieber et al., 2024). Scattering from nanoparticles is particularly challenging, and can artificially increase rates of light absorbance. We therefore recommend that future studies recognize and discuss the potential influence of light scattering when interpreting light absorbance measurements. In this work, we also conducted a sensitivity analysis of the light scattering from nanoparticles (Sect. S8). Particle concentrations below the detection limits of nanoparticle tracking analysis or dynamic light scattering can produce errors over 100 % in calculated absorbance rates (Fig. S17). These findings indicate that calculated rates of light absorbance, and consequently, $^1O_2^*$ quantum yields, may be sensitive to scattering artifacts an introduce an additional source of uncertainty.

4 Recommendations

Reproducible and comparable quantification of $^1O_2^*$ in atmospheric systems requires attention to experimental design and data analysis. Previously measured R_{abs} for environmental samples are on the order of 10^{-6} to 10^{-5} $\mathrm{mol_{photons}\,L^{-1}\,s^{-1}}$ for fog water samples (Kaur and Anastasio, 2017) and for PM extracts in multiple studies (Bogler et al., 2022; Kaur et al., 2019b; Petersen-Sonn et al., 2025; Ma et al., 2023a). $[^1O_2^*]_{\mathrm{SS}}$ measured from particulate matter (PM) extracts using chemical probe-based methods have been reported in the range of 10^{-14} to 10^{-12} M and depend strongly on the extract concentration (Kaur et al., 2019a; Leresche et al., 2021; Lyu et al., 2023; Ma et al., 2024; Manfrin et al., 2019; Bogler et al., 2022).

However, direct comparisons of R_{abs} and $[^1O_2^*]_{\mathrm{SS}}$ across different studies are complicated by differences in photoreactor light output, which dictate the magnitude of these parameters. $^1O_2^*$ quantum yield ($\Phi_{^1O_2^*}$) offers a more comparable metric, as it normalizes for photon flux and photosensitizer concentration. Previously reported $\Phi_{^1O_2^*}$ values from atmospheric samples range from 0.002 to up to 0.19, highlighting the large range of $\Phi_{^1O_2^*}$ values for more complex systems (Petersen-Sonn et al., 2025; Ma et al., 2023a; Kaur et al., 2019b; Bogler et al., 2022; Manfrin et al., 2019; Ma et al., 2024; Lyu et al., 2023).

Based on this intercomparison, we make the following recommendations to improve the reproducibility and interpretation of atmospheric $^1O_2^*$ measurements across experimental setups:

1. *Considering wavelength dependence:* Excited state oxidant studies should explicitly report the irradiation wavelengths used. At a minimum, spectrophotometer measurements and action spectra of light absorbance should be included. Without this information, it can be difficult to interpret results across different studies or to evaluate the influence of wavelength-dependence on reported apparent quantum yields.

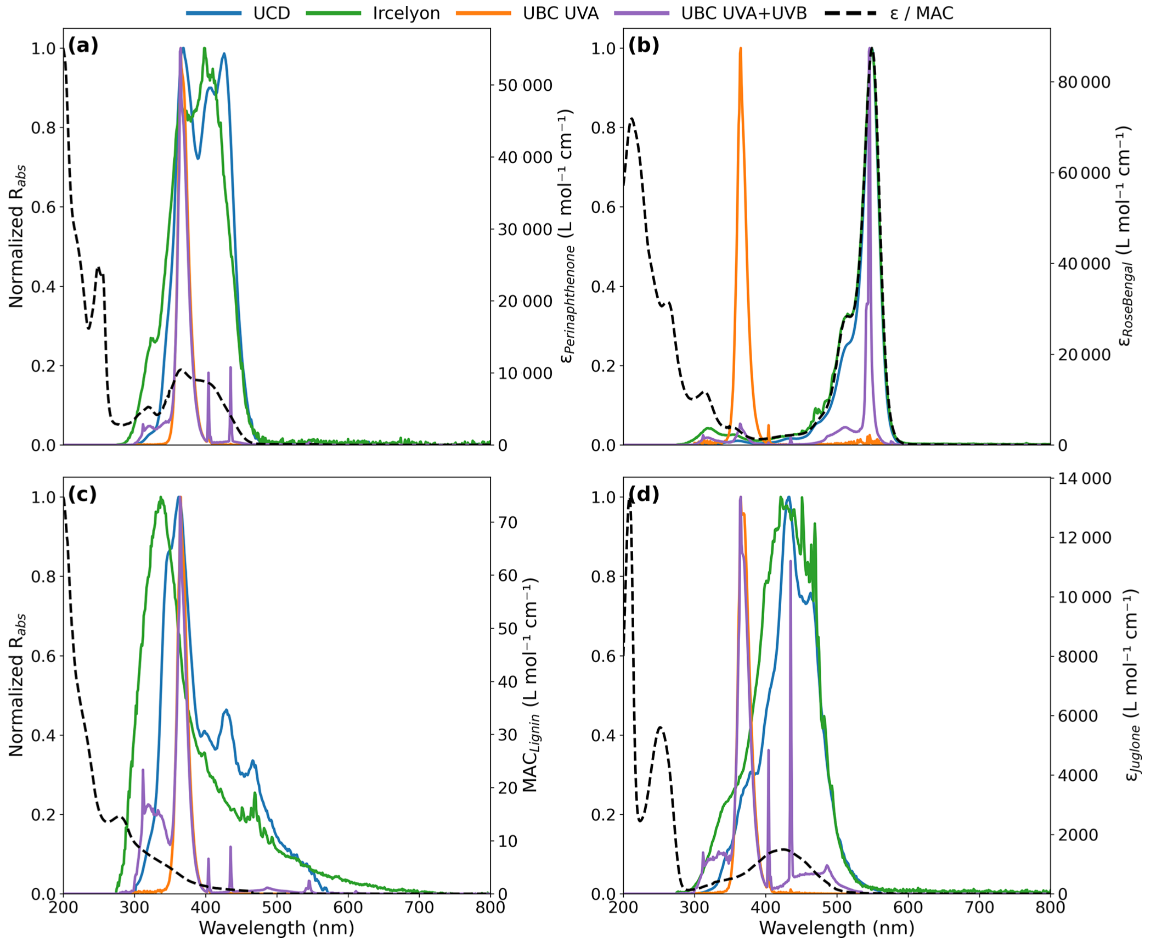

Figure 5. Normalized to peak for each photoreactor set up individually (i.e., peak value = 1) wavelength-distributed rate of light absorbance for **(a)** perinaphthenone, **(b)** Rose Bengal, **(c)** lignin, and **(d)** juglone for all four photoreactor setups from three different labs (UCD, Ircelyon, UBC). Molar absorption coefficients are shown as black dashed lines and correspond to the right *y*-axis for all compounds. Wavelength-distributed rate of light absorbance is calculated using the form of Eq. (1) prior to summation.

2. *Chemical probe concentration:* We recommend using concentrations of furfuryl alcohol such that the reaction of $^1O_2^*$ with the probe accounts for less than 1 % of the total $^1O_2^*$ loss, ensuring that the probe does not perturb steady-state $^1O_2^*$ concentrations. This condition can be evaluated by calculating the fraction of $^1O_2^*$ lost to FFA relative to other sinks (Sect. S13), which corresponds to $[FFA]_0 < 27$ µM (at 25 °C).

3. *Control and report the temperature of photoreactor:* We recommend that photoreactor setups be temperature controlled to avoid deviation from the temperature-dependent rate constant of furfuryl alcohol with $^1O_2^*$ (Appiani et al., 2017). Our use of a range of 20–25 °C is based on practically achievable temperature control across cooling systems. UCD and Ircelyon's water cooling system is more precise than UBC's liquid N_2 through the copper coil system. In addition, there are temperature effects beyond furfuryl alcohol's rate constant, likely involving impacts on the photophysics of the excitation (Figs. S18, S19).

4. *Light scattering considerations:* When working with particulate matter extracts, solutions may contain insoluble material which can scatter light during a UV/Vis spectrometry measurement. Thus, the impact of light scattering should be considered when calculating rates of light absorbance, as scattering can artificially increase apparent absorbance by accounting for scattered light.

5. *Control experiments:* Experiments should include a sample without a photosensitizer to evaluate direct chemical probe decay, and a sample without light to assess probe degradation in the dark (Fig. S1). Adding an •OH radical quencher is also important to mitigate furfuryl alcohol decay due to other oxidants. Additionally, experiments conducted in the absence of oxygen are necessary to determine whether the chemical probe

reacts directly with the $^3C^*$, particularly in atmospheric contexts where nitroaromatic compounds can react with furfuryl alcohol (Sect. 3.3.1, Fig. S14). However, results from purged and deoxygenated experiments should be interpreted with caution, as the removal of oxygen may fundamentally alter the system, for example by increasing $^3C^*$ lifetimes and allowing other reaction pathways to emerge. Experiments using deuterated water can test for kinetic solvent isotope effects, providing additional confirmation that furfuryl alcohol decay arises primarily from $^1O_2^*$. Although it is not possible to completely isolate the reaction of $^1O_2^*$ with furfuryl alcohol, these controls enhance the reliability and intercomparability of $^1O_2^*$ quantification.

In addition to the recommendations outlined above, several design features should be considered when constructing new photoreactor systems. The ideal photoreactor would include:

1. an irradiance spectrum that spans a broad range of wavelengths, attempting to reproduce the solar spectrum, such as a xenon lamp
2. temperature control over a wide range
3. the ability to process a high number of samples.

As highlighted in Sect. 3.2, to extrapolate laboratory measurements to the atmosphere, the use of natural sunlight is an advantage. We note that solar irradiance is not constant in either intensity or spectral distribution, as it varies with solar zenith angle and season. Although irradiation sources that span wavelength ranges similar to those of natural sunlight can help reduce wavelength dependent quantum yield artifacts, it remains difficult to perfectly reproduce solar radiation under laboratory conditions. While xenon lamps replicate the solar spectral distribution well, they are point sources and therefore cannot accommodate high throughput experiments. Alternatives such as multi-bulb or LED systems (Wu et al., 2021) in photoreactors such as the Rayonet increase throughput but struggle to span wavelength ranges similar to that of the solar spectrum. Incubator-style photoreactors have also been developed (Anton et al., 2024), though they may not provide uniform photon flux across all samples. Short pathlength photoreactors have also recently been developed (Niedek et al., 2026), which reduce light attenuation in strongly absorbing solutions by minimizing optical pathlength while maintaining temperature control. These trade offs highlight the need to balance spectral accuracy, photon flux intensity, and sample throughput depending on the research objectives.

5 Atmospheric implications

Forest fires release chromophoric species to the atmosphere, and photochemically-generated oxidants, including $^3C^*$ and $^1O_2^*$, can drive multiphase atmospheric chemistry. Recent laboratory and field studies have demonstrated that steady-state concentrations of $^1O_2^*$ in atmospheric waters and aerosol liquid water often exceed those of •OH by two to three orders of magnitude, particularly in particulate phases enriched in BrC (Ma et al., 2023a; Manfrin et al., 2019). Under these conditions, $^1O_2^*$ can dominate the oxidation of specific compound classes, including N-containing compounds and S-containg compounds (Manfrin et al., 2019). $^1O_2^*$ is also the dominant oxidant over $^3C^*$ and •OH for amino acids and carboxamides (Petersen-Sonn et al., 2025). Furans in BrC can also be oxidized by $^1O_2^*$ to form SOA (Arciva et al., 2025). $^1O_2^*$ therefore impacts organic aerosol aging, aqueous SOA formation, and BrC evolution.

Quantitative comparisons of $^1O_2^*$ across studies remain challenging due to methodological differences in probe and actinometer selection, light source, light normalization, and competing sinks for the probe, the sensitizer and $^1O_2^*$. Consequently, variability in reported $^1O_2^*$ concentrations can span orders of magnitude even for similar particle types, limiting our ability to select a concentration or quantum yield as inputs for constraining models. Nevertheless, Zhang et al. (2024) parameterized $^3C^*$ and $^1O_2^*$ as functions of dissolved organic carbon and light absorption to predict secondary organic aerosol formation from wildfire smoke phenols. The authors highlighted how the uncertain in $^1O_2^*$ steady-state concentrations was a limitation in their study. The intercomparison presented here addresses this gap by systematically evaluating commonly used $^1O_2^*$ quantification approaches under controlled yet atmospherically relevant conditions. By establishing this best-practice guide for probe choice, control experiments, calibrations, actinometry, wavelength-dependent quantum yields and and uncertainty reporting, this work enables more robust inter-study comparisons and facilitates integration of $^1O_2^*$ chemistry into multiphase chemical models. Ultimately, we need to better constrain the concentrations of $^1O_2^*$ and $^3C^*$ generated from different types of BrC to better predict aerosol photochemical aging.

Furthermore, photochemical experiments for quantifying $^1O_2^*$ are conducted in bulk solutions and are therefore not representative of concentrated organic aerosols. Kaur et al. (2019b) and Ma et al. (2021) have estimated that $^1O_2^*$ is likely underestimated in particulate matter as the concentration of chromophores increases, despite adding organic matter as sinks for $^1O_2^*$. There is also an ongoing need to identify unique sensitizers relevant for the atmosphere such as nitrophenols in BrC, (Fleming et al., 2020; Siemens et al., 2023) to further understand the drivers of excited state oxidants in aerosols. In addition, Chang et al. (2025) used structure-activity relationships and machine learning approaches to predict $^3C^*$ and $^1O_2^*$ and identified photosensitizer properties, intersystem crossing yields and triplet-state energies as sources of uncertainty. We hope that our intercomparison study addresses this need by harmonizing methodologies for quantifying $^1O_2^*$, enabling closer integration between predictive photosensitizer models and multiphase atmospheric chemistry simulations.

Data availability. All data collected and used in this study are available in the Supplement (Tables S1–S4).

Supplement. The supplement related to this article is available online at https://doi.org/10.5194/amt-19-3961-2026-supplement.

Author contributions. NBD, EAPS, & LMDH conceptualized the study with contributions from CG and CA. KJG & CS conducted measurements at UBC, LMDH conducted measurements at UC Davis, and EAPS & ZG conducted measurements at Ircelyon. KJG conducted the phosphorescence measurements at U of Calgary with support from NMO and BH. KJG and NBD wrote the manuscript with contributions from all authors.

Competing interests. The contact author has declared that none of the authors has any competing interests.

Acknowledgements. The authors thank Benjamin Herring for their support with the HPLC and UV-Vis instruments at UBC. The authors acknowledge preliminary experiments by Chloé Arthozoul and Denise Chew at UBC.

Financial support. This research was funded by the University of British Columbia, including a 4-Year Fellowship for KJG, and the Natural Sciences and Engineering Council of Canada (NSERC). The authors also acknowledge support from the French National Research Agency under the grant agreement SENSOX (grant no. ANR-22-CE01-0023), the University of Lyon 1, and the US National Science Foundation (grant no. 2220307).

Review statement. This paper was edited by Yoshiteru Iinuma and reviewed by two anonymous referees.

References

Akherati, A., He, Y., Garofalo, L. A., Hodshire, A. L., Farmer, D. K., Kreidenweis, S. M., Permar, W., Hu, L., Fischer, E. V., Jen, C. N., Goldstein, A. H., Levin, E. J. T., DeMott, P. J., Campos, T. L., Flocke, F., Reeves, J. M., Toohey, D. W., Pierce, J. R., and Jathar, S. H.: Dilution and photooxidation driven processes explain the evolution of organic aerosol in wildfire plumes, Environ. Sci.: Atmos., 2, 1000–1022, https://doi.org/10.1039/D1EA00082A, 2022.

Albinet, A., Minero, C., and Vione, D.: Photochemical generation of reactive species upon irradiation of rainwater: Negligible photoactivity of dissolved organic matter, Sci. Total Environ., 408, 3367–3373, https://doi.org/10.1016/j.scitotenv.2010.04.011, 2010.

Anastasio, C. and McGregor, K. G.: Chemistry of fog waters in California's Central Valley: 1. In situ photoformation of hydroxyl radical and singlet molecular oxygen, Atmos. Environ., 35, 1079–1089, https://doi.org/10.1016/S1352-2310(00)00281-8, 2001.

Anton, L. d. B., Silverman, A. I., and Apell, J. N.: Determining wavelength-dependent quantum yields of photodegradation: importance of experimental setup and reference values for actinometers, Environ. Sci.-Proc. Imp., 26, 1052–1063, https://doi.org/10.1039/D4EM00084F, 2024.

Appiani, E., Ossola, R., Latch, D. E., Erickson, P. R., and McNeill, K.: Aqueous singlet oxygen reaction kinetics of furfuryl alcohol: effect of temperature, pH, and salt content, Environ. Sci.-Proc. Imp., 19, 507–516, https://doi.org/10.1039/C6EM00646A, 2017.

Arakaki, T., Anastasio, C., Kuroki, Y., Nakajima, H., Okada, K., Kotani, Y., Handa, D., Azechi, S., Kimura, T., Tsuhako, A., and Miyagi, Y.: A General Scavenging Rate Constant for Reaction of Hydroxyl Radical with Organic Carbon in Atmospheric Waters, Environ. Sci. Technol., 47, 8196, https://doi.org/10.1021/es401927b, 2013.

Arciva, S., Zhou, Y., Jiang, W., Ross, A., Zhang, Q., and Anastasio, C.: Aqueous Oxidation of Biomass-Burning Furans by Singlet Molecular Oxygen (1O2*), Environ. Sci. Technol., 59, 10357–10367, https://doi.org/10.1021/acs.est.4c10778, 2025.

Armarego, W. L. F. and Chai, C.: Chapter 4 – Purification of Organic Chemicals, in: Purification of Laboratory Chemicals (Seventh Edition), edited by: Armarego, W. L. F. and Chai, C., Butterworth-Heinemann, Boston, 103–554, ISBN 978-0-12-382161-4, https://doi.org/10.1016/B978-0-12-382161-4.00004-2, 2013.

Bieber, P., Darwish, G. H., Algar, W. R., and Borduas-Dedekind, N.: The presence of nanoparticles in aqueous droplets containing plant-derived biopolymers plays a role in heterogeneous ice nucleation, J. Chem. Phys., 161, 094304, https://doi.org/10.1063/5.0213171, 2024.

Bogler, S., Daellenbach, K. R., Bell, D. M., Prévôt, A. S. H., El Haddad, I., and Borduas-Dedekind, N.: Singlet Oxygen Seasonality in Aqueous PM10 is Driven by Biomass Burning and Anthropogenic Secondary Organic Aerosol, Environ. Sci. Technol., 56, 15389–15397, https://doi.org/10.1021/acs.est.2c04554, 2022.

Borduas-Dedekind, N., Gemmell, K. J., Madri Jayakody, M., Lee, R. J. M., Sardena, C., and Zala, S.: Singlet oxygen is produced from brown carbon-containing cooking organic aerosols (BrCOA) under indoor lighting, Environ. Sci.: Atmos., 4, 611–619, https://doi.org/10.1039/D3EA00167A, 2024.

Bregnhøj, M., Westberg, M., Jensen, F., and Ogilby, P. R.: Solvent-dependent singlet oxygen lifetimes: temperature effects implicate tunneling and charge-transfer interactions, Phys. Chem. Chem. Phys., 18, 22946–22961, https://doi.org/10.1039/C6CP01635A, 2016.

Burnett, A. I., Wiseman, C. L. S., and Styler, S. A.: Photochemical Production of Singlet Oxygen by Toronto Road Dust, Environ. Sci. Technol., 59, 19377–19386, https://doi.org/10.1021/acs.est.4c09631, 2025.

Chang, Y., Liang, Z., Qin, Y., Zhou, L., and Chan, C. K.: Profiling the Photosensitizing Properties of Atmospheric Brown Carbon, ACS ES&T Air, 2, 2081–2091, https://doi.org/10.1021/acsestair.5c00098, 2025.

Cole, C. A., Carlsten, C., Koehle, M., and Brauer, M.: Particulate matter exposure and health impacts of urban cyclists: A randomized crossover study, Environ. Health, https://doi.org/10.1186/s12940-018-0424-8, 2018.

Cote, C. D., Schneider, S. R., Lyu, M., Gao, S., Gan, L., Holod, A. J., Chou, T. H. H., and Styler, S. A.: Photochemical Production of Singlet Oxygen by Urban Road Dust, Environ. Sci. Technol. Lett., 5, 92–97, https://doi.org/10.1021/acs.estlett.7b00533, 2018.

Davis, C. A., McNeill, K., and Janssen, E. M.-L.: Non-Singlet Oxygen Kinetic Solvent Isotope Effects in Aquatic Photochemistry, Environ. Sci. Technol., 52, 9908–9916, https://doi.org/10.1021/acs.est.8b01512, 2018.

Dhaini, B., Wagner, L., Moinard, M., Daouk, J., Arnoux, P., Schohn, H., Schneller, P., Acherar, S., Hamieh, T., Frochot, C., Dhaini, B., Wagner, L., Moinard, M., Daouk, J., Arnoux, P., Schohn, H., Schneller, P., Acherar, S., Hamieh, T., and Frochot, C.: Importance of Rose Bengal Loaded with Nanoparticles for Anti-Cancer Photodynamic Therapy, Pharmaceuticals, 15, https://doi.org/10.3390/ph15091093, 2022.

Drozd, G. T., Weltzin, T., Skiffington, S., Lee, D., Valiev, R., Kurtén, T., Madison, L. R., He, Y., and Gargano, L.: Wavelength-resolved quantum yields for vanillin photochemistry: self-reaction and ionic-strength implications for wildfire brown carbon lifetime, Environ. Sci.: Atmos., 4, 509–518, https://doi.org/10.1039/D4EA00002A, 2024.

Du, Z., He, Y., Fan, J., Fu, H., Zheng, S., Xu, Z., Qu, X., Kong, A., and Zhu, D.: Predicting apparent singlet oxygen quantum yields of dissolved black carbon and humic substances using spectroscopic indices, Chemosphere, 194, 405–413, https://doi.org/10.1016/j.chemosphere.2017.11.172, 2018.

Dulin, D. and Mill, T.: Development and evaluation of sunlight actinometers, Environ. Sci. Technol., 16, 815–820, https://doi.org/10.1021/es00105a017, 1982.

Durantini, A. M. and Greer, A.: Interparticle Delivery and Detection of Volatile Singlet Oxygen at Air/-Solid Interfaces, Environ. Sci. Technol., 55, 3559–3567, https://doi.org/10.1021/acs.est.0c07922, 2021.

Durantini, A. M., Lapoot, L., Jabeen, S., Ghosh, G., Bipu, J., Essang, S., Singh, B. C., and Greer, A.: Tuning the 1O2 Oxidation of a Phenol at the Air/Solid Interface of a Nanoparticle: Hydrophobic Surface Increases Oxophilicity, Langmuir, 39, 11134–11144, https://doi.org/10.1021/acs.langmuir.3c01676, 2023.

Erickson, P. R., Moor, K. J., Werner, J. J., Latch, D. E., Arnold, W. A., and McNeill, K.: Singlet Oxygen Phosphorescence as a Probe for Triplet-State Dissolved Organic Matter Reactivity, Environ. Sci. Technol., 52, 9170–9178, https://doi.org/10.1021/acs.est.8b02379, 2018.

Faust, B. C. and Allen, J. M.: Aqueous-phase photochemical sources of peroxyl radicals and singlet molecular oxygen in clouds and fog, J. Geophys. Res.-Atmos., 97, 12913–12926, https://doi.org/10.1029/92JD00843, 1992.

Fleming, L. T., Lin, P., Roberts, J. M., Selimovic, V., Yokelson, R., Laskin, J., Laskin, A., and Nizkorodov, S. A.: Molecular composition and photochemical lifetimes of brown carbon chromophores in biomass burning organic aerosol, Atmos. Chem. Phys., 20, 1105–1129, https://doi.org/10.5194/acp-20-1105-2020, 2020.

Galbavy, E. S., Ram, K., and Anastasio, C.: 2-Nitrobenzaldehyde as a chemical actinometer for solution and ice photochemistry, J. Photoch. Photobio. A, 209, 186–192, https://doi.org/10.1016/j.jphotochem.2009.11.013, 2010.

George, C., Ammann, M., D'Anna, B., Donaldson, D. J., and Nizkorodov, S. A.: Heterogeneous Photochemistry in the Atmosphere, Chem. Rev., 115, 4218–4258, https://doi.org/10.1021/cr500648z, 2015.

Gianotti, E., Martins Estevão, B., Cucinotta, F., Hioka, N., Rizzi, M., Renò, F., and Marchese, L.: An Efficient Rose Bengal Based Nanoplatform for Photodynamic Therapy, Chemistry, 20, 10921–10925, https://doi.org/10.1002/chem.201404296, 2014.

Go, B. R., Lyu, Y., Ji, Y., Li, Y. J., Huang, D. D., Li, X., Nah, T., Lam, C. H., and Chan, C. K.: Aqueous secondary organic aerosol formation from the direct photosensitized oxidation of vanillin in the absence and presence of ammonium nitrate, Atmos. Chem. Phys., 22, 273–293, https://doi.org/10.5194/acp-22-273-2022, 2022.

Go, B. R., Li, Y. J., Huang, D. D., and Chan, C. K.: Aqueous-Phase Photoreactions of Mixed Aromatic Carbonyl Photosensitizers Yield More Oxygenated, Oxidized, and less Light-Absorbing Secondary Organic Aerosol (SOA) than Single Systems, Environ. Sci. Technol., 58, 7924–7936, https://doi.org/10.1021/acs.est.3c10199, 2024.

Gollnick, K., Franken, T., Schade, G., and Dörhöfer, G.: Photosensitized Oxygenation as a Function of the Triplet Energy of Sensitizers, Ann. NY Acad. Sci., 171, 89–107, https://doi.org/10.1111/j.1749-6632.1970.tb39307.x, 1970.

Gottschalk, P., Paczkowski, J., and Neckers, D. C.: Factors influencing the quantum yields for rose bengal formation of singlet oxygen, J. Photochem., 35, 277–281, https://doi.org/10.1016/0047-2670(86)87059-9, 1986.

Haag, W. R., Hoigné, J., Gassman, E., and Braun, A.: Singlet oxygen in surface waters – Part I: Furfuryl alcohol as a trapping agent, Chemosphere, 13, 631–640, https://doi.org/10.1016/0045-6535(84)90199-1, 1984.

Heinlein, L. M. D., He, J., Sunday, M. O., Guo, F., Campbell, J., Moon, A., Kapur, S., Fang, T., Edwards, K., Cesler-Maloney, M., Burns, A. J., Dibb, J., Simpson, W., Shiraiwa, M., Alexander, B., Mao, J., Flynn III, J. H., Stutz, J., and Anastasio, C.: Surprisingly robust photochemistry in subarctic particles during winter: evidence from photooxidants, Atmos. Chem. Phys., 25, 9561–9581, https://doi.org/10.5194/acp-25-9561-2025, 2025.

Hems, R. F., Schnitzler, E. G., Liu-Kang, C., Cappa, C. D., and Abbatt, J. P.: Aging of Atmospheric Brown Carbon Aerosol, ACS Earth Space Chem., 5, 722–748, https://doi.org/10.1021/acsearthspacechem.0c00346, 2021.

Kabanov, V., Ghosh, S., Lovell, J. F., and Heyne, B.: Singlet oxygen partition between the outer-, inner- and membrane-phases of photo/chemotherapeutic liposomes, Phys. Chem. Chem. Phys., 21, 25054–25064, https://doi.org/10.1039/C9CP05159G, 2019.

Kaur, R. and Anastasio, C.: Light absorption and the photoformation of hydroxyl radical and singlet oxygen in fog waters, Atmos. Environ., 164, 387–397, https://doi.org/10.1016/j.atmosenv.2017.06.006, 2017.

Kaur, R. and Anastasio, C.: First Measurements of Organic Triplet Excited States in Atmospheric Waters, Environ. Sci. Technol., 52, 5218, https://doi.org/10.1021/acs.est.7b06699, 2018.

Kaur, R., Hudson, B. M., Draper, J., Tantillo, D. J., and Anastasio, C.: Aqueous reactions of organic triplet excited states with atmospheric alkenes, Atmos. Chem. Phys., 19, 5021–5032, https://doi.org/10.5194/acp-19-5021-2019, 2019a.

Kaur, R., Labins, J. R., Helbock, S. S., Jiang, W., Bein, K. J., Zhang, Q., and Anastasio, C.: Photooxidants from brown carbon and other chromophores in illuminated particle extracts, Atmos. Chem. Phys., 19, 6579–6594, https://doi.org/10.5194/acp-19-6579-2019, 2019b.

Klein, G. W., Bhatia, K., Madhavan, V., and Schuler, R. H.: Reaction of hydroxyl radicals with benzoic acid. Isomer distribution in the radical intermediates, J. Phys. Chem., 79, 1767–1774, https://doi.org/10.1021/j100584a005, 1975.

Laskin, A., Laskin, J., and Nizkorodov, S. A.: Chemistry of Atmospheric Brown Carbon, Chem. Rev., 115, 4335, https://doi.org/10.1021/cr5006167, 2015.

Laszakovits, J. R., Berg, S. M., Anderson, B. G., O'Brien, J. E., Wammer, K. H., and Sharpless, C. M.: p-Nitroanisole/pyridine and p-nitroacetophenone/pyridine actinometers revisited: Quantum yield in comparison to ferrioxalate, Environ. Sci. Technol. Lett., 4, 11–14, https://doi.org/10.1021/acs.estlett.6b00422, 2017.

Lee, H. J. J., Aiona, P. K., Laskin, A., Laskin, J., and Nizkorodov, S. A.: Effect of Solar Radiation on the Optical Properties and Molecular Composition of Laboratory Proxies of Atmospheric Brown Carbon, Environ. Sci. Technol., 48, 10217–10226, https://doi.org/10.1021/es502515r, 2014.

Lee, R. J. M., Akande, A. A., Kamal, S., Heine, P. A., Padhiar, P., Tonkin, D., Rusinoff, W., Rezaei, M., and Borduas-Dedekind, N.: The UBC ATMOX chamber: An 8 m^3 LED-powered modular environmental chamber for indoor and outdoor atmospheric chemistry, EGUsphere [preprint], https://doi.org/10.5194/egusphere-2025-3041, 2025.

Leresche, F., Salazar, J. R., Pfotenhauer, D. J., Hannigan, M. P., Majestic, B. J., and Rosario-Ortiz, F. L.: Photochemical Aging of Atmospheric Particulate Matter in the Aqueous Phase, Environ. Sci. Technol., 55, 13152–13163, https://doi.org/10.1021/acs.est.1c00978, 2021.

Li, F., Lv, J., He, A., Xu, J., Zhao, L., Wang, X., Mao, L., Li, S., Wang, H., Wang, Y., and Jiang, G.: Unexpected Generation of Singlet Oxygen at the Air–Water Interface of Aqueous Microdroplets, J. Am. Chem. Soc., 147, 30574–30581, https://doi.org/10.1021/jacs.5c02431, 2025a.

Li, J., Chen, Q., and Guan, D.: Insights into the triplet photochemistry of atmospheric aerosol and subfractions isolated with different polarity, Atmos. Environ., 290, 119375, https://doi.org/10.1016/j.atmosenv.2022.119375, 2022.

Li, Y., Fu, T.-M., Yu, J. Z., Zhang, A., Yu, X., Ye, J., Zhu, L., Shen, H., Wang, C., Yang, X., Tao, S., Chen, Q., Li, Y., Li, L., Che, H., and Heald, C. L.: Nitrogen dominates global atmospheric organic aerosol absorption, Science, 387, 989–995, https://doi.org/10.1126/science.adr4473, 2025b.

Liu, Y., Li, Y., Chan, W. L., Bao, Y., Lee, P. K. H., and Nah, T.: Efficient Production of Reactive Oxidants by Atmospheric Bacterial-Derived Organic Matter in the Aqueous Phase, Environ. Sci. Technol., 59, 6757–6770, https://doi.org/10.1021/acs.est.5c01526, 2025.

Lyu, Y., Lam, Y. H., Li, Y., Borduas-Dedekind, N., and Nah, T.: Seasonal variations in the production of singlet oxygen and organic triplet excited states in aqueous $PM_{2.5}$ in Hong Kong SAR, South China, Atmos. Chem. Phys., 23, 9245–9263, https://doi.org/10.5194/acp-23-9245-2023, 2023.

Ma, L., Guzman, C., Niedek, C., Tran, T., Zhang, Q., and Anastasio, C.: Kinetics and Mass Yields of Aqueous Secondary Organic Aerosol from Highly Substituted Phenols Reacting with a Triplet Excited State, Environ. Sci. Technol., 55, 5772–5781, https://doi.org/10.1021/acs.est.1c00575, 2021.

Ma, L., Worland, R., Jiang, W., Niedek, C., Guzman, C., Bein, K. J., Zhang, Q., and Anastasio, C.: Predicting photooxidant concentrations in aerosol liquid water based on laboratory extracts of ambient particles, Atmos. Chem. Phys., 23, 8805–8821, https://doi.org/10.5194/acp-23-8805-2023, 2023a.

Ma, L., Worland, R., Tran, T., and Anastasio, C.: Evaluation of Probes to Measure Oxidizing Organic Triplet Excited States in Aerosol Liquid Water, Environ. Sci. Technol., 57, 6052–6062, https://doi.org/10.1021/acs.est.2c09672, 2023b.

Ma, L., Worland, R., Heinlein, L., Guzman, C., Jiang, W., Niedek, C., Bein, K. J., Zhang, Q., and Anastasio, C.: Seasonal variations in photooxidant formation and light absorption in aqueous extracts of ambient particles, Atmos. Chem. Phys., 24, 1–21, https://doi.org/10.5194/acp-24-1-2024, 2024.

Madhiyan, M. and Moor, K. J.: Singlet Oxygen Quantum Yields: Comparing Chemical Probe and Time-Resolved Phosphorescence, Environ. Sci. Technol., 60, 8051–8061, https://doi.org/10.1021/acs.est.5c08242, 2026.

Maizel, A. C., Li, J., and Remucal, C. K.: Relationships Between Dissolved Organic Matter Composition and Photochemistry in Lakes of Diverse Trophic Status, Environ. Sci. Technol., 51, 9624–9632, https://doi.org/10.1021/acs.est.7b01270, 2017.

Manfrin, A., Nizkorodov, S. A., Malecha, K. T., Getzinger, G. J., McNeill, K., and Borduas-Dedekind, N.: Reactive Oxygen Species Production from Secondary Organic Aerosols: The Importance of Singlet Oxygen, Environ. Sci. Technol., 53, 8553–8562, https://doi.org/10.1021/acs.est.9b01609, 2019.

Marchisio, A., Minella, M., Maurino, V., Minero, C., and Vione, D.: Photogeneration of reactive transient species upon irradiation of natural water samples: Formation quantum yields in different spectral intervals, and implications for the photochemistry of surface waters, Water Res., 73, 145–156, https://doi.org/10.1016/j.watres.2015.01.016, 2015.

McNeill, K. and Canonica, S.: Triplet state dissolved organic matter in aquatic photochemistry: reaction mechanisms, substrate scope, and photophysical properties, Environ. Sci.-Proc. Imp., 18, 1381–1399, https://doi.org/10.1039/C6EM00408C, 2016.

Mir, M., Jansen, L. M. G., Wilkinson, F., Bourdelande, J. L., and Marquet, J.: Efficiency of singlet oxygen generation from the triplet states of nitrophenyl ethers, J. Photoch. Photobio. A, 113, 113–117, https://doi.org/10.1016/S1010-6030(97)00325-0, 1998.

Myers-Pigg, A. N., Griffin, R. J., Louchouarn, P., Norwood, M. J., Sterne, A., and Cevik, B. K.: Signatures of Biomass Burning Aerosols in the Plume of a Saltmarsh Wildfire in South Texas, Environ. Sci. Technol., 50, 9308–9314, https://doi.org/10.1021/acs.est.6b02132, 2016.

Niedek, C., Jiang, W., Zhang, A., Anastasio, C., and Zhang, Q.: A novel short-pathlength photoreactor to study aqueous-phase photochemistry: application to biomass-burning phenols, Atmos. Meas. Tech., 19, 2009–2023, https://doi.org/10.5194/amt-19-2009-2026, 2026.

Nonell, S. and Flors, C.: Steady-state and time-resolved singlet oxygen phosphorescence detection in the near-IR, Singlet Oxygen. Applications in Biosciences and Nanosciences, Vol. 2, Royal Society of Chemistry, 7–26, https://doi.org/10.1039/9781782626992-00007, 2016.

Ossola, R., Jönsson, O. M., Moor, K., and McNeill, K.: Singlet Oxygen Quantum Yields in Environmental Waters, Chem. Rev., 121, 4100–4146, https://doi.org/10.1021/acs.chemrev.0c00781, 2021.

Partanen, S. B., Erickson, P. R., Latch, D. E., Moor, K. J., and McNeill, K.: Dissolved Organic Matter Singlet Oxygen Quantum Yields: Evaluation Using Time-Resolved Singlet Oxygen Phosphorescence, Environ. Sci. Technol., 54, 3316–3324, https://doi.org/10.1021/acs.est.9b07246, 2020.

Partanen, S. B., Apell, J. N., Lin, J., and McNeill, K.: Factors affecting the mixed-layer concentrations of singlet oxygen in sunlit lakes, Environ. Sci.-Proc. Imp., 23, 1130–1145, https://doi.org/10.1039/D1EM00062D, 2021.

Petersen-Sonn, E. A., Brigante, M., Deguillaume, L., Jaffrezo, J.-L., Perrier, S., and George, C.: Evaluating the potential secondary contribution of photosensitized chemistry to OH production in aqueous aerosols, Environ. Sci.: Atmos., 4, 1170–1182, https://doi.org/10.1039/D4EA00103F, 2024.

Petersen-Sonn, E. A., Brigante, M., Deguillaume, L., Jaffrezo, J.-L., and George, C.: Tropospheric Multiphase Chemistry: Excited Triplet States Compete with OH Radicals and Singlet Molecular Oxygen, ACS Earth Space Chem., 9, 533–544, https://doi.org/10.1021/acsearthspacechem.4c00295, 2025.

Redmond, R. W. and Gamlin, J. N.: A Compilation of Singlet Oxygen Yields from Biologically Relevant Molecules, Photochem. Photobiol., 70, 391–475, https://doi.org/10.1111/j.1751-1097.1999.tb08240.x, 1999.

Samburova, V., Connolly, J., Gyawali, M., Yatavelli, R. L. N., Watts, A. C., Chakrabarty, R. K., Zielinska, B., Moosmüller, H., and Khlystov, A.: Polycyclic aromatic hydrocarbons in biomass-burning emissions and their contribution to light absorption and aerosol toxicity, Sci. Total Environ., 568, 391–401, https://doi.org/10.1016/j.scitotenv.2016.06.026, 2016.

Schmidt, R., Tanielian, C., Dunsbach, R., and Wolff, C.: Phenalenone, a universal reference compound for the determination of quantum yields of singlet oxygen O2(1Δg) sensitization, J. Photoch. Photobio. A, 79, 11–17, https://doi.org/10.1016/1010-6030(93)03746-4, 1994.

Schweitzer, C. and Schmidt, R.: Physical Mechanisms of Generation and Deactivation of Singlet Oxygen, Chem. Rev., 103, 1685–1758, https://doi.org/10.1021/cr010371d, 2003.

Schweitzer, C., Mehrdad, Z., Noll, A., Grabner, E.-W., and Schmidt, R.: Mechanism of Photosensitized Generation of Singlet Oxygen during Oxygen Quenching of Triplet States and the General Dependence of the Rate Constants and Efficiencies of O2(1Σg+), O2(1Δg), and O2(3Σg-) Formation on Sensitizer Triplet State Energy and Oxidation Potential, J. Phys. Chem. A, 107, 2192–2198, https://doi.org/10.1021/jp026189d, 2003.

Shakya, K. M., Louchouarn, P., and Griffin, R. J.: Lignin-Derived Phenols in Houston Aerosols: Implications for Natural Background Sources, Environ. Sci. Technol., 45, 8268–8275, https://doi.org/10.1021/es201668y, 2011.

Sharpless, C. M.: Lifetimes of Triplet Dissolved Natural Organic Matter (DOM) and the Effect of NaBH4 Reduction on Singlet Oxygen Quantum Yields: Implications for DOM Photophysics, Environ. Sci. Technol., 46, 4466–4473, https://doi.org/10.1021/es300217h, 2012.

Siemens, K. S. A., Pagonis, D., Guo, H., Schueneman, M. K., Dibb, J. E., Campuzano-Jost, P., Jimenez, J. L., and Laskin, A.: Probing Atmospheric Aerosols by Multimodal Mass Spectrometry Techniques: Revealing Aging Characteristics of Its Individual Molecular Components, ACS Earth Space Chem., https://doi.org/10.1021/acsearthspacechem.3c00228, 2023.

Smith, J. D., Sio, V., Yu, L., Zhang, Q., and Anastasio, C.: Secondary Organic Aerosol Production from Aqueous Reactions of Atmospheric Phenols with an Organic Triplet Excited State, Environ. Sci. Technol., 48, 1049–1057, https://doi.org/10.1021/es4045715, 2014.

Smith, J. D., Kinney, H., and Anastasio, C.: Phenolic carbonyls undergo rapid aqueous photodegradation to form low-volatility, light-absorbing products, Atmos. Environ., 126, 36–44, https://doi.org/10.1016/j.atmosenv.2015.11.035, 2016.

Tymstra, C., Stocks, B. J., Cai, X., and Flannigan, M. D.: Wildfire management in Canada: Review, challenges and opportunities, Progress in Disaster Science, 5, 100045, https://doi.org/10.1016/j.pdisas.2019.100045, 2020.

Valiev, R. R., He, Y., Weltzin, T., Zhu, A., Lee, D., Moore, E., Gee, A., Drozd, G., and Kurten, T.: Wavelength-dependent intersystem crossing dynamics of phenolic carbonyls in wildfire emissions, Phys. Chem. Chem. Phys., 27, 998–1007, https://doi.org/10.1039/D4CP03501A, 2025.

Vallon, M., Gao, L., Jiang, F., Krumm, B., Nadolny, J., Song, J., Leisner, T., and Saathoff, H.: LED-based solar simulator to study photochemistry over a wide temperature range in the large simulation chamber AIDA, Atmos. Meas. Tech., 15, 1795–1810, https://doi.org/10.5194/amt-15-1795-2022, 2022.

Wilkinson, F., Helman, W. P., and Ross, A. B.: Quantum Yields for the Photosensitized Formation of the Lowest Electronically Excited Singlet State of Molecular Oxygen in Solution, J. Phys. Chem. Ref. Data, 22, 113–262, https://doi.org/10.1063/1.555934, 1993.

Wu, B., Liu, T., Wang, Y., Zhao, G., Chen, B., and Chu, C.: High Sample Throughput LED Reactor for Facile Characterization of the Quantum Yield Spectrum of Photochemically Produced Reactive Intermediates, Environ. Sci. Technol., https://doi.org/10.1021/acs.est.1c04608, 2021.

Xu, J., Cui, T., Fowler, B., Fankhauser, A., Yang, K., Surratt, J. D., and McNeill, V. F.: Aerosol Brown Carbon from Dark Reactions of Syringol in Aqueous Aerosol Mimics, ACS Earth Space Chem., 2, 608, https://doi.org/10.1021/acsearthspacechem.8b00010, 2018.

Xu, J., Hettiyadura, A. P. S., Liu, Y., Zhang, X., Kang, S., and Laskin, A.: Atmospheric Brown Carbon on the Tibetan Plateau: Regional Differences in Chemical Composition and Light Absorption Properties, Environ. Sci. Technol. Lett., 9, 219–225, https://doi.org/10.1021/acs.estlett.2c00016, 2022.

Zhang, J., Shrivastava, M., Ma, L., Jiang, W., Anastasio, C., Zhang, Q., and Zelenyuk, A.: Modeling Novel Aqueous Particle and Cloud Chemistry Processes of Biomass Burning Phenols and Their Potential to Form Secondary Organic Aerosols, Environ. Sci. Technol., 58, 3776–3786, https://doi.org/10.1021/acs.est.3c07762, 2024.

Zheng, P., Chen, Y., Wang, Z., Liu, Y., Pu, W., Yu, C., Xia, M., Xu, Y., Guo, J., Guo, Y., Tian, L., Qiao, X., Huang, D. D., Yan, C., Nie, W., Worsnop, D. R., Lee, S., and Wang, T.: Molecular Characterization of Oxygenated Organic Molecules and Their Dominating Roles in Particle Growth in Hong Kong, Environ. Sci. Technol., 57, 7764–7776, https://doi.org/10.1021/acs.est.2c09252, 2023.

Zhou, X., Davis, A. J., Kieber, D. J., Keene, W. C., Maben, J. R., Maring, H., Dahl, E. E., Izaguirre, M. A., Sander, R., and Smoydzyn, L.: Photochemical production of hydroxyl radical and hydroperoxides in water extracts of nascent marine aerosols produced by bursting bubbles from Sargasso seawater, Geophys. Res. Lett., 35, https://doi.org/10.1029/2008GL035418, 2008.